

Fifth order finite volume WENO in general orthogonally–curvilinear coordinates

Mohammad Afzal Shadab^{a,1,*}, Dinshaw Balsara^{b,2}, Wei Shyy^{a,3}, Kun Xu^{a,c,4}

^a*Department of Mechanical and Aerospace Engineering, Hong Kong University of Science and Technology, Clear Water Bay, Peninsula, Hong Kong*

^b*Department of Physics, University of Notre Dame, Indiana, United States IN 46556-5670*

^c*Department of Mathematics, Hong Kong University of Science and Technology, Clear Water Bay, Peninsula, Hong Kong*

Abstract

High order reconstruction in the finite volume (FV) approach is achieved by a more fundamental form of the fifth order WENO reconstruction in the framework of orthogonally–curvilinear coordinates, for solving the hyperbolic conservation equations. The derivation employs a piecewise parabolic polynomial approximation to the zone averaged values (\bar{Q}_i) to reconstruct the right, middle, and left interface values (q_i^+ , q_i^M and q_i^- respectively). The grid dependent linear weights of the WENO are recovered by inverting a Vandermonde–like linear system of equations with spatially varying coefficients. A scheme for calculating the linear weights, optimal weights, and smoothness indicator on a regularly– and irregularly–spaced grid in orthogonally–curvilinear coordinates is proposed. A grid independent relation for evaluating the smoothness indicator is derived from the basic definition. Finally, the procedures for the source term integration

*Corresponding author

Email addresses: `mashadab@connect.ust.hk` (Mohammad Afzal Shadab), `dbalsara@nd.edu` (Dinshaw Balsara), `weishyy@ust.hk` (Wei Shyy), `makxu@ust.hk` (Kun Xu)

¹Research Postgraduate Student, Department of Mechanical and Aerospace Engineering, Hong Kong University of Science and Technology, Clear Water Bay, Hong Kong

²Professor, Department of Physics, University of Notre Dame, Indiana, United States IN 46556-5670

³Provost and Chair Professor, Department of Mechanical and Aerospace Engineering, Hong Kong University of Science and Technology, Clear Water Bay, Hong Kong

⁴Chair Professor, Department of Mechanical and Aerospace Engineering and Department of Mathematics, Hong Kong University of Science and Technology, Clear Water Bay, Hong Kong

and extension to multi-dimensions are proposed. Analytical values of the linear and optimal weights, and also the weights required for the source term integration and flux averaging, are provided for a regularly-spaced grid in Cartesian, cylindrical, and spherical coordinates. Conventional fifth order WENO reconstruction for the regularly-spaced grids in the Cartesian coordinates can be fully recovered in the case of limiting curvature ($R \rightarrow \infty$). The fifth order finite volume WENO-C (orthogonally-curvilinear version of WENO) reconstruction scheme is tested for several 1D and 2D benchmark test cases involving smooth and discontinuous flows in cylindrical and spherical coordinates.

Keywords: Fifth order, WENO, Cartesian, Cylindrical, Spherical, Structured grids, Multidimensional reconstruction

1. Introduction

Finite volume weighted essentially non-oscillatory (WENO) reconstruction scheme represents the state of art numerical methods in one- (1D) and two-dimensional (2D) hyperbolic conservation laws [1, 2, 3, 4, 5]. Although finite volume methods are more expensive than the finite difference schemes, they represent better versions of conservation laws, since they deal with the volume averages instead of the point values, which changes only when there is an imbalance of the fluxes across the finite volume [2]. Flux evaluation at the interface requires an important task of reconstructing the cell averaged value at interface [2]. High order reconstruction is preferred for the cases of complex flow phenomena including discontinuous flows, smooth flows with turbulence [6], aeroacoustics [6], and magnetohydrodynamics (MHD) [7, 8, 9]. In a plethora of reconstruction techniques including p^{th} order accurate essentially non-oscillatory (ENO) scheme [10], second order total variation diminishing (TVD) methods [2], discontinuous Galerkin methods [6], and modified piecewise parabolic method (PPM) [2, 11, 12, 13], WENO stands a chance by its virtue of attaining a convexly optimized $(2p - 1)^{th}$ order of convergence for smooth flows aided with a novel ENO strategy for maintaining high order accuracy even for

the discontinuous flows [2, 10].

The conventional WENO scheme is specifically designed for the reconstruction in Cartesian coordinates on uniform grids [3, 4]. For arbitrary curvilinear mesh, the procedure of using a Jacobian, in order to map a general curvilinear mesh to a uniform Cartesian mesh, is employed [10]. However, it might be an unphysical approach since the complex flow phenomena occurring in the original system might not be represented correctly by the reconstruction in the transformed coordinates [2]. It is indeed a better choice to reconstruct the cell averaged variables in their original coordinates rather than mapping it to a Cartesian mesh, in order to preserve a higher order accuracy [2]. The reconstruction in general coordinates can be performed with the aid of two techniques: genuine multidimensional reconstruction and dimension-by-dimension reconstruction [10]. Genuine multidimensional reconstruction is computationally expensive and highly complex since it considers all of the finite volumes while constructing the polynomial [10]. A better approach is to perform a dimension-by-dimension reconstruction since it consists of less expensive one-dimensional sweeps in every dimension and most of the problems of engineering interests are considered in orthogonally-curvilinear coordinates like Cartesian, cylindrical, and spherical coordinates with regularly- and irregularly-spaced grids. A breakthrough in the arena of high order reconstruction in these coordinates is the application of the Vandermode-like linear systems of equations with spatially varying coefficients [2]. It is reintroduced in the present work to build a basis for the derivation of the high order WENO schemes. However, Mignone [2] restricted the work to the usage of the third order WENO approach with the weight functions provided by Yamaleev and Carpenter [14] and did not extend the work to multi-dimensions (2D and 3D). Modified piecewise parabolic method (PPM₅) gave better results when compared with the modified third order WENO, provided in [2]. However, the latter reconstruction scheme gives consistent values for all the numerical tests performed. Moreover, there is a drop of accuracy of the modified third order WENO scheme in the discontinuous flows [2], when the standard nonlinear weights derived by Jiang and Shu [3] are used because they

are specifically restricted to the Cartesian grids.

The motivation for the present work is to develop a general approach for the fifth order finite volume WENO–C reconstruction scheme in orthogonally–curvilinear coordinates involving regularly– and irregularly–spaced grids, from the original ideas of linear weight evaluation by Mignone [2], and optimal weights, smoothness indicators by Jiang and Shu [3]. Also, the present work provides a computationally efficient extension of this scheme to multi–dimensions and renders dealing with the source terms simple and straightforward.

The present work is divided into four sections. Section 2 includes the fifth order finite volume WENO–C reconstruction procedure for a regularly– and irregularly–spaced grid in orthogonally–curvilinear coordinates. This section is further subdivided into seven subsections, starting from the basic formulation of the discretized hyperbolic conservation law in the curvilinear coordinates. Then, the linear weights and optimal weights are derived in the most general form for orthogonally–curvilinear coordinates and are provided for the case of regularly–spaced mesh in Cartesian, cylindrical and spherical coordinates. Next, the smoothness indicators are derived by minimizing the L_2 –norm of the derivatives of the reconstruction polynomials, equivalent to the idea of minimizing the total variation for the approximations, which is a good measurement for smoothness [3]. Then, a general procedure for the source term integration is formulated and the resulting weights are provided for the regularly–spaced structured grids. Next, the mechanism for extending this scheme to multi–dimensions is proposed. Finally, a complete algorithm for the implementation of WENO–C reconstruction scheme in 3D is presented. This scheme is applicable to any general regularly– and irregularly–spaced grid in orthogonally–curvilinear coordinates, but the weights are provided only for the standard cases of regularly–spaced grids in Cartesian, cylindrical, and spherical coordinates except for the spherical–meridional coordinate due to its complexity. A simple formulation for evaluating the smoothness indicator is proposed for all kinds of mesh in orthogonally–curvilinear coordinates. In addition, the method of attack for irregularly–spaced grids is discussed briefly in the corre-

sponding sections. It is followed by the section 3 in which diverse 1D and 2D numerical benchmark tests involving smooth and discontinuous flows in cylindrical and spherical coordinates are presented. Finally, section 4 concludes the paper.

2. Fifth order finite volume WENO–C reconstruction

2.1. Finite volume discretization in curvilinear coordinates

The scalar conservation law in an orthogonal system of coordinates (x_1, x_2, x_3) having the scale factors h_1, h_2, h_3 and unit vectors $(\hat{\mathbf{e}}_1, \hat{\mathbf{e}}_2, \hat{\mathbf{e}}_3)$ in the respective directions, is provided in Eq. (1).

$$\frac{\partial Q}{\partial t} + \nabla \cdot \mathbf{F} = S \quad (1)$$

where Q is the conserved quantity of the fluid, $\mathbf{F} = (F_1, F_2, F_3)$ is the corresponding flux vector, and S is the source term. The divergence operator is further expressed in the form of Eq. (2).

$$\nabla \cdot \mathbf{F} = \frac{1}{h_1 h_2 h_3} \left[\frac{\partial}{\partial x_1} (h_2 h_3 F_1) + \frac{\partial}{\partial x_2} (h_1 h_3 F_2) + \frac{\partial}{\partial x_3} (h_1 h_2 F_3) \right] \quad (2)$$

The Eq. (1) is discretized over a computational domain comprising of $N_1 \times N_2 \times N_3$ cells in the corresponding directions with the grid sizes given in Eq. (3).

$$\Delta x_{1,i} = x_{1,i+\frac{1}{2}} - x_{1,i-\frac{1}{2}}, \quad \Delta x_{2,j} = x_{2,j+\frac{1}{2}} - x_{2,j-\frac{1}{2}}, \quad \Delta x_{3,k} = x_{3,k+\frac{1}{2}} - x_{3,k-\frac{1}{2}} \quad (3)$$

For the sake of simplicity, the notation (i, j, k) is mentioned as \mathbf{i} where $\mathbf{i} \in \mathbb{Z}^3$; and \mathbb{Z}^3 is a vector of coordinate index in the computational domain with $1 \leq i \leq N_1$, $1 \leq j \leq N_2$, and $1 \leq k \leq N_3$. Also, the position of the cell interface orthogonal to any direction (d) is given by $\hat{\mathbf{e}}_d$, and it is denoted by $\mathbf{i} \pm \frac{1}{2} \hat{\mathbf{e}}_d$ e.g. $\mathbf{i} \pm \frac{1}{2} \hat{\mathbf{e}}_1$ refers to the $i \pm \frac{1}{2}$ interfaces of the cell \mathbf{i} in $\hat{\mathbf{e}}_1$ direction. The cell volume

is given in Eq. (4).

$$\Delta\mathcal{V}_{i,j,k} = \int_{x_{3,k-\frac{1}{2}}}^{x_{3,k+\frac{1}{2}}} \int_{x_{2,j-\frac{1}{2}}}^{x_{2,j+\frac{1}{2}}} \int_{x_{1,i-\frac{1}{2}}}^{x_{1,i+\frac{1}{2}}} h_1 h_2 h_3 dx_1 dx_2 dx_3 \quad (4)$$

The flux F_d is averaged over the surface—area (A_d) of the interface in $\hat{\mathbf{e}}_d$ direction and is formulated for $\mathbf{i} + \frac{1}{2}\hat{\mathbf{e}}_1$ in Eq. (5).

$$\tilde{F}_{1,\mathbf{i}+\frac{1}{2}\hat{\mathbf{e}}_1} = \frac{1}{A_{1,\mathbf{i}+\frac{1}{2}\hat{\mathbf{e}}_1}} \int_{x_{3,k-\frac{1}{2}}}^{x_{3,k+\frac{1}{2}}} \int_{x_{2,j-\frac{1}{2}}}^{x_{2,j+\frac{1}{2}}} F_1 h_2 h_3 dx_2 dx_3 \quad (5)$$

where the cross—sectional area $A_{1,\mathbf{i}+\frac{1}{2}\hat{\mathbf{e}}_1}$ is provided in Eq. (6). Here the scale factors h_2, h_3 are the functions of the position vector at the interface $\mathbf{i} + \frac{1}{2}\hat{\mathbf{e}}_1$.

$$A_{1,\mathbf{i}+\frac{1}{2}\hat{\mathbf{e}}_1} = \int_{x_{3,k-\frac{1}{2}}}^{x_{3,k+\frac{1}{2}}} \int_{x_{2,j-\frac{1}{2}}}^{x_{2,j+\frac{1}{2}}} h_2 h_3 dx_2 dx_3 \quad (6)$$

Similarly, the expressions for the other directions ($d = 2, 3$) can be obtained by cyclic permutations. The final form of the discretized conservation law can be derived by integrating Eq. (1) over the cell volume and applying the Gauss theorem to the flux term yielding Eq. (7), where $\bar{Q}_{\mathbf{i}}$ and $\bar{S}_{\mathbf{i}}$ are the conservative variable and the source term averaged over the finite volume \mathbf{i} .

$$\frac{\partial}{\partial t} \bar{Q}_{\mathbf{i}} + \frac{1}{\Delta\mathcal{V}_{\mathbf{i}}} \sum_d \left[(A_d \tilde{F}_d)_{\mathbf{i}+\frac{1}{2}\hat{\mathbf{e}}_d} - (A_d \tilde{F}_d)_{\mathbf{i}-\frac{1}{2}\hat{\mathbf{e}}_d} \right] = \bar{S}_{\mathbf{i}} \quad (7)$$

In cylindrical coordinates, $(x_1, x_2, x_3) \equiv (R, \theta, z)$ and $(h_1, h_2, h_3) \equiv (1, R, 1)$ and Eq. (7) transforms to Eq. (8).

$$\begin{aligned} \frac{\partial}{\partial t} \bar{Q}_{\mathbf{i}} = & - \frac{(\tilde{F}_R R)_{\mathbf{i}+\frac{1}{2}\hat{\mathbf{e}}_r} - (\tilde{F}_R R)_{\mathbf{i}-\frac{1}{2}\hat{\mathbf{e}}_r}}{\Delta\mathcal{V}_{R,i}} - \frac{(\tilde{F}_\theta)_{\mathbf{i}+\frac{1}{2}\hat{\mathbf{e}}_\theta} - (\tilde{F}_\theta)_{\mathbf{i}-\frac{1}{2}\hat{\mathbf{e}}_\theta}}{R_i \Delta\theta_j} \\ & - \frac{(\tilde{F}_z)_{\mathbf{i}+\frac{1}{2}\hat{\mathbf{e}}_z} - (\tilde{F}_z)_{\mathbf{i}-\frac{1}{2}\hat{\mathbf{e}}_z}}{\Delta z_k} + \bar{S}_{\mathbf{i}} \end{aligned} \quad (8)$$

where the $(\tilde{F}_R, \tilde{F}_\theta, \tilde{F}_z)$ are the surface averaged flux vector (\mathbf{F}) components in the (R, θ, z) directions and $\Delta\mathcal{V}_{R,i} = (R_{i+\frac{1}{2}}^2 - R_{i-\frac{1}{2}}^2)/2$ is the cell radial volume.

In spherical coordinates $(x_1, x_2, x_3) \equiv (r, \theta, \phi)$ and $(h_1, h_2, h_3) \equiv (1, r, r \sin \theta)$ and Eq. (7) transforms to Eq. (9).

$$\begin{aligned} \frac{\partial}{\partial t} \bar{Q}_i = & - \frac{(\tilde{F}_r r^2)_{i+\frac{1}{2}} \hat{\mathbf{e}}_r - (\tilde{F}_r r^2)_{i-\frac{1}{2}} \hat{\mathbf{e}}_r}{\Delta \mathcal{V}_{r,i}} - \frac{(\tilde{F}_\theta \sin \theta)_{i+\frac{1}{2}} \hat{\mathbf{e}}_\theta - (\tilde{F}_\theta \sin \theta)_{i-\frac{1}{2}} \hat{\mathbf{e}}_\theta}{\tilde{r}_i \Delta \mu_j} \\ & - \frac{\Delta \theta_j}{\Delta \mu_j} \frac{(\tilde{F}_\phi)_{i+\frac{1}{2}} \hat{\mathbf{e}}_\phi - (\tilde{F}_\phi)_{i-\frac{1}{2}} \hat{\mathbf{e}}_\phi}{\tilde{r}_i \Delta \phi_k} + \bar{S}_i \end{aligned} \quad (9)$$

where $(\tilde{F}_r, \tilde{F}_\theta, \tilde{F}_\phi)$ are the surface averaged flux vector components in the (r, θ, ϕ) directions and the remaining geometrical factors are provided in Eq. (10).

$$\Delta \mathcal{V}_{r,i} = \frac{(r_{i+\frac{1}{2}}^3 - r_{i-\frac{1}{2}}^3)}{3}; \quad \tilde{r}_i = \frac{2}{3} \frac{(r_{i+\frac{1}{2}}^3 - r_{i-\frac{1}{2}}^3)}{(r_{i+\frac{1}{2}}^2 - r_{i-\frac{1}{2}}^2)}; \quad \Delta \mu_j = \cos \theta_{j-\frac{1}{2}} - \cos \theta_{j+\frac{1}{2}} \quad (10)$$

2.2. Evaluation of the linear weights

A non-uniform grid spacing with zone width $\Delta \xi_i = \xi_{i+\frac{1}{2}} - \xi_{i-\frac{1}{2}}$ is considered having $\xi \in (x_1, x_2, x_3)$ as the coordinate along the reconstruction direction and $\xi_{i+\frac{1}{2}}$ denoting the location of the cell interface between zones i and $i+1$. Let \bar{Q}_i be the cell average of conserved quantity Q inside zone i at some given time, which can be expressed in form of Eq. (11).

$$\bar{Q}_i = \frac{1}{\Delta \mathcal{V}_i} \int_{\xi_{i-\frac{1}{2}}}^{\xi_{i+\frac{1}{2}}} Q_i(\xi) \frac{\partial \mathcal{V}}{\partial \xi} d\xi \quad (11)$$

where the local cell volume of the i^{th} cell in the direction of reconstruction given in Eq. (12)

$$\Delta \mathcal{V}_i = \int_{\xi_{i-\frac{1}{2}}}^{\xi_{i+\frac{1}{2}}} \frac{\partial \mathcal{V}}{\partial \xi} d\xi \quad (12)$$

$\frac{\partial \mathcal{V}}{\partial \xi}$ is a one-dimensional Jacobian and $\Delta \mathcal{V}_i$ is the local cell volume. The values of $\frac{\partial \mathcal{V}}{\partial \xi}$ for volumetric operations are summarized in the Table 1 for structured grids in standard coordinates.

Table 1: $\frac{\partial \mathcal{V}}{\partial \xi}$ values for the regularly-spaced grids for volumetric operations

<i>Coordinates</i>	<i>Direction(s)</i>	$\frac{\partial \mathcal{V}}{\partial \xi}$
Cartesian	(x, y, z)	ξ^0
Cylindrical	(R)	ξ^1
Cylindrical	(θ, z)	ξ^0
Spherical	(r)	ξ^2
Spherical	(θ)	$\sin \xi$
Spherical	(ϕ)	ξ^0

Now, our aim is to find a p^{th} order accurate approximation to the actual solution by constructing a polynomial distribution within a given zone i , as given in Eq. (13).

$$Q_i(\xi) = a_{i,0} + a_{i,1}(\xi - \xi_i^c) + a_{i,2}(\xi - \xi_i^c)^2 + \dots + a_{i,p-1}(\xi - \xi_i^c)^{p-1} \quad (13)$$

where $a_{i,n}$ corresponds to a vector of the coefficients which to be determined and ξ_i^c can be taken as the cell center. However, the final values at the interface are independent of the particular choice of ξ_i^c and one may as well set $\xi_i^c = 0$ [2]. Unlike the cell center, the centroid is not equidistant from the cell interfaces in the case of curvilinear coordinates and the cell averaged values are assigned at the centroid [2]. Further, the method has to be locally conservative which means that the polynomial $Q_i(\xi)$ must fit the neighboring cell averages, satisfying Eq. (14).

$$\int_{\xi_{i+s-\frac{1}{2}}}^{\xi_{i+s+\frac{1}{2}}} Q_i(\xi) \frac{\partial \mathcal{V}}{\partial \xi} d\xi = \Delta \mathcal{V}_{i+s} \bar{Q}_{i+s} \quad \text{for} \quad -i_L \leq s \leq i_R \quad (14)$$

where the stencil includes i_L cells to the left and i_R cells to the right of the i^{th} zone such that $i_L + i_R + 1 = p$. Using Eqs. (12) and (13) in Eq. (14) and performing manipulation leads to a $p \times p$ linear system in the coefficients $\{a_{i,n}\}$,

given in Eq. (15).

$$\begin{pmatrix} \beta_{i-i_L,0} & \cdots & \beta_{i-i_L,p-1} \\ \vdots & \ddots & \vdots \\ \beta_{i+i_R,0} & \cdots & \beta_{i+i_R,p-1} \end{pmatrix} \begin{pmatrix} a_{i,0} \\ \vdots \\ a_{i,p-1} \end{pmatrix} = \begin{pmatrix} \bar{Q}_{i-i_L} \\ \vdots \\ \bar{Q}_{i+i_R} \end{pmatrix} \quad (15)$$

where

$$\beta_{i+s,n} = \frac{1}{\Delta \mathcal{V}_{i+s}} \int_{\xi_{i+s-\frac{1}{2}}}^{\xi_{i+s+\frac{1}{2}}} (\xi - \xi_i^c)^n \frac{\partial \mathcal{V}}{\partial \xi} d\xi \quad (16)$$

Eq. (15) can be written in the short notation using a $p \times p$ matrix \mathbf{B} with the rows ranging from $s = -i_L, \dots, i_R$ and columns ranging from $n = 0, \dots, p-1$.

$$\sum_{n=0}^{p-1} \mathbf{B}_{sn} a_{i,n} = \bar{Q}_{i+s} \quad (17)$$

However, the evaluation of the weights $a_{i,k}$ in Eqs. (15) and (17) requires the zone averaged values \bar{Q}_i , increasing the computational cost of the whole process as it needs to be evaluated at every time step.

Also, the coefficients $\{a_{i,n}\}$ extracted from Eq. (15) will satisfy the relation (18).

$$q_i^+ = \lim_{\xi \rightarrow \xi_{i+\frac{1}{2}}^{(-)}} Q_i(\xi) = \sum_{n=0}^{p-1} a_{i,n} (\xi_{i+\frac{1}{2}} - \xi_i^c)^n; \quad q_i^- = \lim_{\xi \rightarrow \xi_{i-\frac{1}{2}}^{(+)}} Q_i(\xi) = \sum_{n=0}^{p-1} a_{i,n} (\xi_{i-\frac{1}{2}} - \xi_i^c)^n \quad (18)$$

A more efficient formulation for evaluating the left and right interface values is rewritten as a linear combination of the adjacent cell averaged values [2], as given in Eq. (19).

$$q_i^\pm = \sum_{s=-i_L}^{i_R} w_{i,s}^\pm \bar{Q}_{i+s} \quad (19)$$

From Eq. (17), after inverting the matrix \mathbf{B} , we get relation (20).

$$a_{i,n} = \sum_{s=-i_L}^{i_R} \mathbf{C}_{ns} \bar{Q}_{i+s} \quad (20)$$

where $\mathbf{C} = \mathbf{B}^{-1}$ corresponds to the inverse of the matrix \mathbf{B} .

After combining Eqs. (18) and (20), we get

$$q_i^\pm = \sum_{n=0}^{p-1} \left(\sum_{s=-i_L}^{i_R} \mathbf{C}_{ns} \bar{Q}_{i+s} \right) (\xi_{i\pm\frac{1}{2}} - \xi_i^c)^n = \sum_{s=-i_L}^{i_R} \bar{Q}_{i+s} \left(\sum_{n=0}^{p-1} \mathbf{C}_{ns} (\xi_{i\pm\frac{1}{2}} - \xi_i^c)^n \right) \quad (21)$$

By comparing Eqs. (19) and (21), we can extract the matrix of weights $w_{i,s}^\pm$.

$$w_{i,s}^\pm = \sum_{n=0}^{p-1} \mathbf{C}_{ns} (\xi_{i\pm\frac{1}{2}} - \xi_i^c)^n \quad (22)$$

Since, $\mathbf{C}_{ns} = (\mathbf{C}^T)_{\mathbf{sn}} = ((\mathbf{B}^T)^{-1})_{\mathbf{sn}}$, Eq. (22) can be finally written in the form of Eq. (23).

$$\sum_{s=-i_L}^{i_R} (\mathbf{B}^T)_{ns} w_{i,s}^\pm = (\xi_{i\pm\frac{1}{2}} - \xi_i^c)^n \quad (23)$$

Therefore, it is evident that the weights $w_{i,s}^\pm$ are shown to satisfy Eq. (24) [2], which is the fundamental equation for reconstruction in orthogonally–curvilinear coordinates.

$$\begin{pmatrix} \beta_{i-i_L,0} & \cdots & \beta_{i-i_L,p-1} \\ \vdots & \ddots & \vdots \\ \beta_{i+i_R,0} & \cdots & \beta_{i+i_R,p-1} \end{pmatrix}^T \begin{pmatrix} w_{i,-i_L}^\pm \\ \vdots \\ w_{i,i_R}^\pm \end{pmatrix} = \begin{pmatrix} 1 \\ \vdots \\ (\xi_{i\pm\frac{1}{2}} - \xi_i^c)^{p-1} \end{pmatrix} \quad (24)$$

Also, the grid dependent linear weights ($w_{i,s}^\pm$) satisfy the normalization condition (25)[2].

$$\sum_{s=-i_L}^{i_R} w_{i,s}^\pm = 1 \quad (25)$$

A number of important remarks pertaining to the fifth order finite volume WENO–C reconstruction are as follows:

1. Eq. (24) is capable of evaluating the grid generated linear weights for any regularly– and irregularly–spaced mesh in orthogonally–curvilinear coordinates. It is observed that these weights are independent of the mesh size for standard regularly–spaced grid cases, but depend on the grid type. Also, they can be evaluated and stored (at a nominal cost) independently

before the actual computation, after the grid type: Cartesian, cylindrical, spherical coordinates, etc, and regularly– and irregularly–spaced grid, is finalized.

2. For the fifth order WENO, three sets of third order ($p = 3$) stencils (S_k) are chosen namely

- $S_0(i - 2, i - 1, i) :: -i_L = 2, i_R = 0$
- $S_1(i - 1, i, i + 1) :: -i_L = 1, i_R = 1$
- $S_2(i, i + 1, i + 2) :: -i_L = 0, i_R = 2.$

In addition to this, another symmetric stencil $S_5 :: (i - 2, i - 1, i, i + 1, i + 2)$ is used to extract the values of the optimal weights in the subsection 2.3.

3. The final interface values (19) and the linear weights depend only on the order of the reconstruction polynomial and not on ξ_i^c , which can be set to zero [2].
4. The values are simplified when the Jacobian is a simple power of ξ i.e. $\frac{\partial \mathcal{V}}{\partial \xi} = \xi^m$. Then, $\beta_{i+s,n}$ of Eq. (16) can be written in the simplified form (26).

$$\beta_{i+s,n} = \frac{m+1}{n+m+1} \frac{\xi_{i+s+\frac{1}{2}}^{n+m+1} - \xi_{i+s-\frac{1}{2}}^{n+m+1}}{\xi_{i+s+\frac{1}{2}}^{m+1} - \xi_{i+s-\frac{1}{2}}^{m+1}} \quad (26)$$

5. For the spherical–meridional coordinate, $\beta_{i+s,n}$ of Eq. (16) becomes highly complex as $(\frac{\partial \mathcal{V}}{\partial \xi} = \sin \xi)$. The value of $\beta_{i+s,n}$ can be computed from Eq. (27) and needs to be solved numerically e.g. by using LU decomposition method.

$$\beta_{i+s,n} = \frac{1}{\cos \xi_{i_s-} - \cos \xi_{i_s+}} \sum_{k=0}^n k! \binom{n}{k} \left[\xi_{i_s-}^{n-k} \cos \left(\xi_{i_s-} + \frac{k\pi}{2} \right) - \xi_{i_s+}^{n-k} \cos \left(\xi_{i_s+} + \frac{k\pi}{2} \right) \right] \quad (27)$$

where $i_{s\pm}$ refers to $i + s \pm \frac{1}{2}$.

6. For irregularly-spaced grids, $\frac{\partial \mathcal{V}}{\partial \xi}$ is not a simple function, which makes the direct integration highly complex and time consuming. Therefore, such cases are tackled using numerical integration of the Eq. (16) and then matrix inversion of the Eq. (24).
7. Eq. (24) can also be used to compute the point-values of $Q(\xi)$ at any other points than the interfaces e.g. the cell center (q_i^M). The value at the cell center is obtained by setting the right hand side of the matrix (24) as $(1, 0, 0, \dots, 0)^T$ with $\xi_i^c = 0$ and is important in the case of nonlinear systems of equations where the reconstruction of the primitive variables is done instead of the conserved variables [2].
8. The linear positive (w_i^+), middle (w_i^M) and negative (w_i^-) weights for the WENO reconstruction for the standard cases of regularly-spaced grid in Cartesian, cylindrical, and spherical coordinates are summarized in the Appendix A.1.1, Appendix A.2.1, and Appendix A.3.1 respectively. The analytical solutions for the spherical-meridional coordinate (θ) are highly intricate and thus, not mentioned in this paper as they need to be dealt numerically.

The weights and the stencil are denoted by $w_{i,l,k}^{p\pm}$ and $S_l^{p\pm}$ respectively, where k is sequence of the weight-applied cell with respect to the cell considered for reconstruction (i), p is the order of reconstruction ($p = i_L + i_R + 1$), l is the stencil number, and ‘ \pm ’ represents the positive and negative weights i.e. weights for reconstructing the right (+) and the left (−) interface values respectively. The derivation of middle (mid-value) weights ($w_{i,l,k}^{pM}$) also follow the same procedure.

The reconstructed values $q_{i,l}^{p\pm}$ represents the p^{th} -order reconstructed value at the right (+) or left (−) interface of the i^{th} cell on the stencil l . The formulation for the interpolated values at the interface for the WENO reconstruction are given by the linear system of Eqs. (28), where i_L and i_R depend on the

stencil l .

$$q_{i,l}^{p\pm} = \sum_{s=-i_L}^{i_R} w_{i,l,s}^{p\pm} \bar{Q}_{i+s} \quad (28)$$

2.3. Optimal weights

The weights which optimize the sum of the lower order interpolated variables into a higher order interpolation are known as the optimal weights [3, 4]. For the case of fifth order WENO interpolation, the third order interpolated variables are optimally weighed in order to achieve fifth order accurate interpolated values as given in Eq. (29) for the case of $p = 3$.

$$q_{i,0}^{(2p-1)\pm} = \sum_{l=0}^{p-1} C_{i,l}^{\pm} q_{i,l}^{p\pm} \quad (29)$$

where $C_{i,l}^{\pm}$ is the optimal weight for the positive/negative cases on the i^{th} finite volume. $C_{i,l}^M$ for mid-value weights also follow the same procedure. So, Eqs. (24) and (26) are employed again to calculate the weights for the fifth order ($2p - 1 = 5$) interpolation ($i_L = 2, i_R = 2$) and its analytical values for standard grids are given in Appendix A.1.2, Appendix A.2.2, and Appendix A.3.2. The fifth order interpolated variable at the interface is equated with the sum of optimally weighed third order interpolated variables, as given in Eq. (29). The optimal weights are evaluated by equating the coefficients of \bar{Q} resulting in $(2p - 1)$ equations with p unknowns, namely $C_{i,l}^{\pm}$. For the fifth order WENO-C reconstruction, the case is simplified to a system of linear equations as given in Eq. (30), by selecting \bar{Q}_{i-2} , \bar{Q}_i , and \bar{Q}_{i+2} coefficients to reduce the computational cost.

$$C_{i,0}^{\pm} = \frac{w_{i,0,-2}^{5\pm}}{w_{i,0,-2}^{3\pm}}; \quad C_{i,2}^{\pm} = \frac{w_{i,0,+2}^{5\pm}}{w_{i,2,+2}^{3\pm}}; \quad C_{i,1}^{\pm} = \frac{w_{i,0,0}^{5\pm} - C_{i,0}^{\pm} w_{i,0,0}^{3\pm} - C_{i,2}^{\pm} w_{i,2,0}^{3\pm}}{w_{i,1,0}^{3\pm}} \quad (30)$$

Some remarks regarding the optimal weights are given below:

1. The summation of the optimal weights always yield unity value and their value is independent of the coefficients of \bar{Q} equated in Eq. (29).

2. Since weights are independent of the conserved variables, optimal weight is also a constant for a selected orthogonally–curvilinear mesh and can be computed in advance with a little storage cost.
3. The analytical values in the Cartesian, cylindrical, and spherical–radial coordinates for a regularly–spaced grid are provided in Appendix A.1.3, Appendix A.2.3, and Appendix A.3.3 respectively.
4. The only case where the optimal weights are mirror–symmetric is of the regularly–spaced grid in Cartesian coordinates. The optimal weights are exactly the same as of the conventional fifth order WENO reconstruction [1, 3] in this case and also when $i \rightarrow \infty$ (limiting curvature) in the case of regularly–spaced grid cases in the cylindrical– and spherical–radial coordinates.
5. The weights for the spherical coordinates are much more complex and computationally expensive. For spherical coordinates, it is advised to use the fifth order weights and linear weights to evaluate the optimal weights or use direct numerical operation after mesh generation since the analytical values of optimal weights contains high order (i^{16}) terms. Moreover, the concept of optimal weights can be completely removed with the aid of WENO–AO type modification by Balsara et al. [15] to the present work. However, the present work remains general and provides the backbone to such construction techniques.

2.4. Smoothness indicators and the nonlinear weights

The smoothness indicators are the nonlinear tools employed to differentiate in between a smooth and a discontinuous flow [4, 3] on a stencil. It is employed in order to discard the discontinuous stencils and maintain a high order accuracy even in the discontinuous flows. From the original idea of [3], the present analysis is performed. Jiang and Shu [3] proposed a novel method of evaluating the smoothness indicators ($IS_{i,l}$). Since, for a regularly– and irregularly–spaced grid, ($IS_{i,l}$) varies with the grid index i , therefore we will use ($IS_{i,l}$) later in

this paper. The idea involves minimization of the L_2 -norm of the derivatives of the reconstruction polynomial, thus, emulating the idea of minimizing the total variation of the approximation. The mathematical definition of the smoothness indicator is given in Eq. (31) [1, 3].

$$IS_{i,l} = \sum_{m=1}^{p-1} \int_{\xi_{j-\frac{1}{2}}}^{\xi_{j+\frac{1}{2}}} \left(\frac{d^m}{d\xi^m} Q_{i,l}(\xi) \right)^2 \Delta \xi_i^{2m-1} d\xi, \quad l = 0, \dots, p-1 \quad (31)$$

To evaluate the value of $IS_{i,l}$, a third order polynomial interpolation on the cell i is required for the stencil S_l using positive and negative reconstructed values, as given in Eq. (32).

$$Q_{i,l}(\xi) = a_{i,l,0} + a_{i,l,1}(\xi - \xi_i^c) + a_{i,l,2}(\xi - \xi_i^c)^2 \quad (32)$$

Let $\xi_{i+1/2} - \xi_i^c = \xi_i^+$, $\xi_{i-1/2} - \xi_i^c = -\xi_i^-$, and $\xi_i^+ + \xi_i^- = \Delta \xi_i$. The polynomial will satisfy the constraints (33) for all kinds of finite volumes.

$$\int_{\xi_{i-\frac{1}{2}}}^{\xi_{i+\frac{1}{2}}} Q_{i,l}(\xi) d\xi = \bar{Q}_i, \quad q_{i,l}^\pm = Q_{i,l}(\xi_{i\pm\frac{1}{2}}) \quad (33)$$

Finally, we get the values of the $a_{i,l,0}$, $a_{i,l,1}$, and $a_{i,l,2}$.

$$\begin{aligned} a_{i,l,0} &= \frac{6\bar{Q}_i \xi_i^- \xi_i^+ + q_{i,l}^+ \xi_i^- (\xi_i^- - 2\xi_i^+) + q_{i,l}^- \xi_i^+ (\xi_i^+ - 2\xi_i^-)}{(\xi_i^+ + \xi_i^-)^2} \\ a_{i,l,1} &= \frac{2q_{i,l}^- (\xi_i^- - 2\xi_i^+) - 6\bar{Q}_i (\xi_i^- - \xi_i^+) - 2q_{i,l}^+ (\xi_i^+ - 2\xi_i^-)}{(\xi_i^+ + \xi_i^-)^2} \\ a_{i,l,2} &= 3 \frac{(q_{i,l}^\pm - 2\bar{Q}_i + q_{i,l}^\pm)}{(\xi_i^+ + \xi_i^-)^2} \end{aligned} \quad (34)$$

For the regularly-spaced grids, the values of ξ^+ and ξ^- are constant throughout the grid, which are given below in the standard coordinates, where i is the index number for the radial cases.

- Cartesian coordinates:

$$(x, y, z) \text{ direction: } \xi^+ = \xi^- = \frac{\Delta \xi}{2}$$

- Cylindrical coordinates:

$$\text{Radial } (R) \text{ direction: } \xi^+ = \Delta R \left(\frac{1}{2} - \frac{1}{12i-6} \right), \quad \xi^- = \Delta R \left(\frac{1}{2} + \frac{1}{12i-6} \right)$$

where $i = \Delta R / R_{i+1/2}$

$$(\theta, z) \text{ direction: } \xi^+ = \xi^- = \frac{\Delta \xi}{2}$$

- Spherical coordinates:

$$\text{Radial } (r) \text{ direction: } \xi^+ = \Delta r \left(\frac{1}{2} - \frac{2i-1}{4(3i^2-3i+1)} \right), \xi^- = \Delta r \left(\frac{1}{2} + \frac{2i-1}{4(3i^2-3i+1)} \right)$$

where $i = \Delta r / r_{i+1/2}$

$$\text{Meridional } (\theta) \text{ direction: } \xi^+ = \theta_{i+\frac{1}{2}} - \theta_i^c, \xi^- = -(\theta_i^c - \theta_{i-\frac{1}{2}})$$

$$\text{where } \theta_i^c = \frac{\theta_{i-\frac{1}{2}} \cos \theta_{i-\frac{1}{2}} - \sin \theta_{i-\frac{1}{2}} - \theta_{i+\frac{1}{2}} \cos \theta_{i+\frac{1}{2}} + \sin \theta_{i+\frac{1}{2}}}{\cos \theta_{i-\frac{1}{2}} - \cos \theta_{i+\frac{1}{2}}}$$

$$(\phi) \text{ direction: } \xi^+ = \xi^- = \frac{\Delta \phi}{2}$$

These values on a regularly-spaced grid in Cartesian coordinates i.e. $\xi^+ = \xi^- = \frac{\Delta \xi}{2}$ transform the relation (33) into the one given in [16].

Now, putting the values of $a_{i,l,0}$, $a_{i,l,1}$, and $a_{i,l,2}$ obtained from Eq. (34) in Eq. (32) and then finally evaluating the smoothness indicator from Eq. (31) yields the following fundamental relation (35) for evaluating the smoothness indicators in fifth order WENO-C reconstruction for a regularly- and irregularly-spaced grid in orthogonally-curvilinear coordinates.

$$IS_{i,l} = 4(39\bar{Q}_i^2 - 39\bar{Q}_i(q_{i,l}^- + q_{i,l}^+) + 10((q_{i,l}^-)^2 + (q_{i,l}^+)^2) + 19q_{i,l}^- q_{i,l}^+) \quad (35)$$

Some remarks regarding the smoothness indicators are as follows:

- Eq. (35) is a general relation in fifth order WENO-C reconstruction for every grid and depends only on the reconstructed variables at the interface (q_i^\pm) .
- q_i^\pm are the third order reconstructed variables obtained from Eq. (28) after using suitable grid dependent linear weights.
- For the regularly-spaced grid case in Cartesian coordinates, the formulation for the fifth order WENO is exactly the same as provided by [1, 3, 16] after the linear weights are substituted.

The nonlinear weight $(\omega_{i,l}^\pm)$ for the WENO-C interpolation is defined as follows [1, 3].

$$\omega_{i,l}^\pm = \frac{\alpha_{i,l}^\pm}{\sum_{l=0}^{p-1} \alpha_{i,l}^\pm} \quad l = 0, 1, 2 \quad (36)$$

where

$$\alpha_{i,l}^{\pm} = \frac{C_{i,l}^{\pm}}{(10^{-6} + IS_{i,l})^2} \quad l = 0, 1, 2 \quad (37)$$

where $C_{i,l}^{\pm}$ is the optimal weight (positive or negative) at i^{th} cell due to l^{th} stencil. The final interpolated interface values are evaluated from the Eq. (38).

$$q_i^{(2p-1)\pm} = \sum_{l=0}^{p-1} \omega_{i,l}^{p\pm} q_{i,l}^{p\pm} \quad (38)$$

2.5. Extension to multi-dimensions

The interface values calculated after the initial application are the point values only when the domain is 1D. For 2D and 3D domains, the reconstructed variables are line and area average values respectively [2, 17, 18]. If these values are employed to evaluate the flux, the scheme drops down to a second order of accuracy [2, 17, 18]. Buchmuller and Helzel [18] proposed a very simple and effective way of achieving the original order of accuracy, just by using one point at each boundary. In this section, we are simply extending their work from Cartesian grids to general grids in orthogonally-curvilinear coordinates.

For the sake of simplicity, a 2D grid in orthogonally-curvilinear coordinates having unit vectors $\hat{\mathbf{e}}_1$ and $\hat{\mathbf{e}}_2$ in the directions is considered, as shown in Fig.1. After reconstructing the left and the right interface averaged values in the first WENO sweep, the second sweep is performed to yield the point values. For the 3D case, line averaged values are yielded at this point and thus, require another reconstruction of line averaged values in the direction orthogonal previous reconstructions to obtain the point values. The Jacobian values for the conversion from volume averaged value to point values are provided in Table 1.

Since this is exactly the same principle as what we have described in Sections 2.2 and 2.3, the theory and derivation are not discussed again. However, this time the line average values are converted to the point values at the mid-point of the interface with the aid of adjacent interfaces' line averaged values. Also, since the quantities have been reconstructed using a WENO scheme in the first face-normal sweep, say blue-colored left face in $\hat{\mathbf{e}}_2$ direction, as shown in

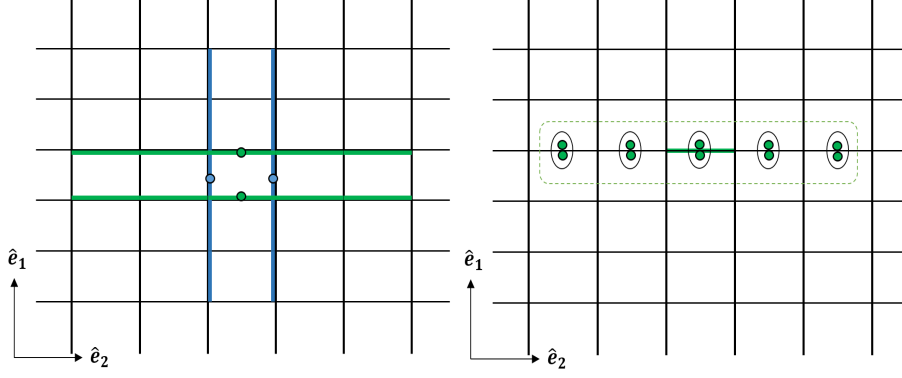


Figure 1: High order interface flux evaluation procedure. Left: Mid-point value reconstruction at each interface inside a cell using adjacent interface average values. Right: Line averaged flux evaluation by solving the Riemann problem at each mid-point and averaging using five adjacent points

Fig.1 (left), the second sweep of interface in the tangential direction $\hat{\mathbf{e}}_1$ doesn't require the complete WENO procedure because it already contains the required smoothness information. Thus, the fifth order accurate weights required for the mid-point value evaluation can be directly calculated by considering ξ in $\hat{\mathbf{e}}_1$ direction with the same fifth order centered stencil, $\xi_i^c = 0$, and substituting ξ_i in place $\xi_{i\pm\frac{1}{2}}$, in Eq. (24). The values of the weights are the same as of the fifth order weights in the corresponding direction as evaluated in Section 2.3. Then, the fluxes can be evaluated from the left and the right hand side conserved variable values at the interface by solving the Riemann problem [19]. In the future, the method will be extended to gas-kinetic scheme (GKS) [20] and unified gas-kinetic scheme (UGKS) [21].

The evaluated fluxes at the mid-points of the interfaces, as shown in Fig. 1 are averaged using polynomial interpolation. In the case of 1D and 2D grids, the Jacobians are supposed to be the unaltered values provided in Table 1. However, for 3D cases, the value of one-dimensional Jacobian is altered according to the situation. Since the final integrated value is a surface averaged value, it is inherently related only to the corresponding two dimensions of that surface. For example while integrating in spherical $(r - \theta)$ plane, the one-dimensional

Jacobians are ξ in r -directional sweep and not ξ^2 ; and unity in θ direction. This is because the averaging procedure is independent of the third dimension ϕ which adds $rd\phi$ term to the integration. So, the altered one-dimensional Jacobians for 2D planar averaging are summarized in Table 2.

Table 2: One-dimensional Jacobian $(\frac{\partial \mathcal{V}}{\partial \xi})$ values for interface flux reconstruction for the regularly-spaced 3D grids

Grid type	Face coordinates $(i - j)$	$\frac{\partial \mathcal{V}_i}{\partial \xi_i}$	$\frac{\partial \mathcal{V}_j}{\partial \xi_j}$
Cartesian	$(x - y), (y - z), (x - z)$	1	1
Cylindrical	$(r - \theta)$	ξ	1
Cylindrical	$(r - z), (\theta - z)$	1	1
Spherical	$(r - \theta), (r - \phi)$	ξ	1
Spherical	$(\theta - \phi)$	$\sin \xi$	1

Consider a p^{th} order accurate polynomial of any variable, say flux Q in this case, joining p consecutive points, say mid-points of the interface as represented in Fig. 1 (right). It can be expressed in the same form as provided in Eq. (13), which takes the matrix form given in Eq. (39).

$$Q_i(\xi) = \begin{pmatrix} 1 & (\xi - \xi_i^c) & \dots & (\xi - \xi_i^c)^{p-1} \end{pmatrix} \begin{pmatrix} a_{i,0} \\ a_{i,1} \\ \vdots \\ a_{i,p-1} \end{pmatrix} \quad (39)$$

But this time, instead of calculating the point values from the line averaged values, vice-versa operation is performed. Eq. (13) is valid for the values from $i - i_L$ (leftmost value) to $i + i_R$ (rightmost value), where $i_L + i_R + 1 = p$. A system of p equations is obtained after substituting the values at each considered

point, the matrix form of which is given in Eq. (40).

$$\begin{pmatrix} Q_{i,-i_L} \\ Q_{i,-i_L+1} \\ \vdots \\ Q_{i,i_R} \end{pmatrix} = \begin{pmatrix} 1 & (\xi_{i-i_L} - \xi_i^c) & \dots & (\xi_{i-i_L} - \xi_i^c)^{p-1} \\ 1 & (\xi_{i-i_L+1} - \xi_i^c) & \dots & (\xi_{i-i_L+1} - \xi_i^c)^{p-1} \\ \vdots & \dots & \ddots & \vdots \\ 1 & (\xi_{i+i_R} - \xi_i^c) & \dots & (\xi_{i+i_R} - \xi_i^c)^{p-1} \end{pmatrix} \begin{pmatrix} a_{i,0} \\ a_{i,1} \\ \vdots \\ a_{i,p-1} \end{pmatrix} \quad (40)$$

where Q is any-arbitrary variable which needs to be averaged in a $[\xi_{i-\frac{1}{2}}, \xi_{i+\frac{1}{2}}]$.

It can be written in a much simpler matrix form given in Eq. (41).

$$[\mathbf{Q}] = [\mathbf{XI}][\mathbf{A}] \quad (41)$$

where $[\mathbf{Q}] = [Q_{i,-i_L}, Q_{i,-i_L+1}, \dots, Q_{i,i_R}]^T$, $[\mathbf{XI}] = \begin{pmatrix} 1 & (\xi_{i-i_L} - \xi_i^c) & \dots & (\xi_{i-i_L} - \xi_i^c)^{p-1} \\ 1 & (\xi_{i-i_L+1} - \xi_i^c) & \dots & (\xi_{i-i_L+1} - \xi_i^c)^{p-1} \\ \vdots & \dots & \ddots & \vdots \\ 1 & (\xi_{i+i_R} - \xi_i^c) & \dots & (\xi_{i+i_R} - \xi_i^c)^{p-1} \end{pmatrix}$

and $[\mathbf{A}] = [a_{i,0}, a_{i,1}, \dots, a_{i,p-1}]^T$

Using the same procedure as described in Sections 2.2 and 2.3 and performing the average of the polynomial as given in Eq. (39) similar to Eq. (11) over the domain $[\xi_{i-1/2}, \xi_{i+1/2}]$, Eq. (42) is obtained.

$$\bar{Q}_i = [\widetilde{\mathbf{XI}}][\mathbf{A}] \quad (42)$$

where $[\widetilde{\mathbf{XI}}] = \left[\frac{1}{\Delta V_i} \int_{\xi_{i-\frac{1}{2}}}^{\xi_{i+\frac{1}{2}}} (\xi - \xi_i^c)^0 \frac{\partial \mathcal{V}}{\partial \xi} d\xi, \frac{1}{\Delta V_i} \int_{\xi_{i-\frac{1}{2}}}^{\xi_{i+\frac{1}{2}}} (\xi - \xi_i^c)^1 \frac{\partial \mathcal{V}}{\partial \xi} d\xi, \dots, \frac{1}{\Delta V_i} \int_{\xi_{i-\frac{1}{2}}}^{\xi_{i+\frac{1}{2}}} (\xi - \xi_i^c)^{p-1} \frac{\partial \mathcal{V}}{\partial \xi} d\xi \right]$

From Eqs. (41) and (42), the final Eq. (43) can be derived, which is the general equation for integration from a lower dimension to a higher dimension.

$$\bar{Q}_i = \{[\widetilde{\mathbf{XI}}][\mathbf{XI}]^{-1}\}[\mathbf{Q}] \quad (43)$$

The term $\{[\widetilde{\mathbf{XI}}][\mathbf{XI}]^{-1}\}$ includes the weights essential for converting the mid-point interface flux values to the line averaged interface flux values, as shown in Fig. 1 (right). The next integration sweep in the transverse direction yields the area-averaged flux values at the interface. The weights for integrations in the corresponding directions are provided in Appendix A.1.4, Appendix

A.2.4, and Appendix A.3.4 for the standard cases. Integration is preferred to be performed in the exact vice-versa fashion as of reconstruction from the surface averages.

2.6. Source term integration

The source terms need to be dealt with extreme accuracy since any contamination in it might deteriorate the high order accuracy. The source term integration is performed based on the works by Mignone [2]. For 1D test cases, it is preferred to reconstruct the mid-point of each cell using WENO procedure, weights of which are provided in the Appendix A.1.5, Appendix A.2.5, and Appendix A.3.5. Reconstructing at Gauss-Lobatto 4 points (4 points, fifth order) instead of mid-point and performing quadrature also yields the same results (not shown in the paper), therefore, mid-point reconstruction with 3 point Simpson quadrature is advised.

The present work is a significant extension to [2] since point values are considered for the source term evaluation, unlike the constant radius averages [2], which yields second order of accuracy only [17, 18]. The theory for deriving the weights for the source term integration is exactly the same as of flux integration given in Section 2.5. However, as the reconstruction of the source-term integration is performed in every dimension, original one-dimensional Jacobians given in Table 1 are used for the reconstruction. If non-radial integration is performed in the first place, ‘ $1/R$ ’ factor in all of the tangential terms at $R = 0$ will yield an infinite value, so only numerators are integrated with the original weights. Moreover, since the source terms contain ‘ $1/R$ ’ factor, the radial integration weights need to be regularized [2], by reconsidering the integration of Eq. (41) with a regularized factor of the source term in Eq. (14) i.e. $\int_{\xi_{i-\frac{1}{2}}}^{\xi_{i+\frac{1}{2}}} \frac{\hat{Q}_i(\xi)}{\xi} \frac{\partial \mathcal{V}}{\partial \xi} d\xi = \Delta \mathcal{V}_i \bar{Q}_i$, where Q represents the original source term (eq. if $Q_i = (p_i/R_i)$, then $\hat{Q}_i = p_i$) in this context.

First integration tangential to the surface is performed in one direction involving five points, to calculate the line average value of the source term. In the next step, five line averaged values are integrated in the transverse direction to

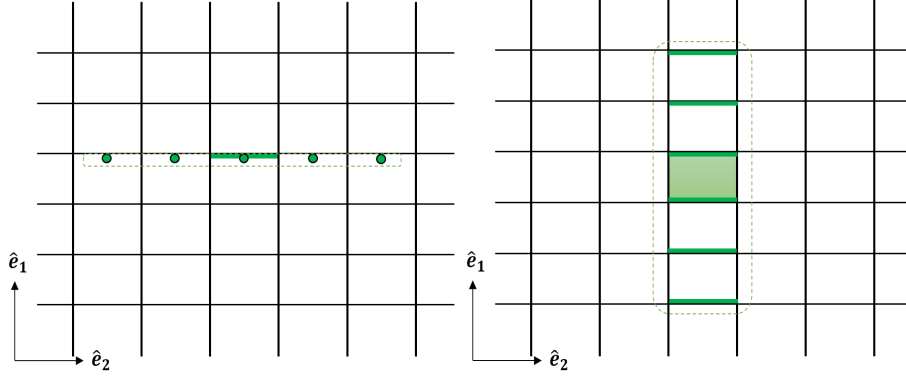


Figure 2: Fifth order source term integration procedure. Left: Fifth order using middle values. Right: Sixth order integration using face values

the first sweep, tangential to the interface as shown in Fig. 2 (left). Finally, a face normal interpolation is performed by utilizing the face averaged source terms of six faces i.e. $(i-5/2)^+$, $(i-3/2)^+$, $(i-1/2)^+$, $(i+1/2)^-$, $(i+3/2)^-$, $(i+5/2)^-$ faces, as illustrated in Fig. 2 (right). The weights for the source term integration are provided for the standard cases in Appendix A.1.5, Appendix A.2.5, and Appendix A.3.5.

In addition to the approach discussed above, interior points can also be used to evaluate the source terms. For 1D tests, it is feasible to utilize the mid-point values and perform Simpson quadrature using the weights given by Mignone [2] and given in the Appendix, to achieve fifth order of accuracy. However, evaluation at the interior points becomes very expensive in multi-dimensions.

2.7. WENO-C final algorithm

The final algorithm for WENO-C reconstruction is as follows:

- After mesh-generation, calculate the values of the linear and optimal weights, fifth order middle (mid-value) interpolation weights, then weights for interface flux and source term integration need to be evaluated in every dimension. For standard cases, weights are provided in the Appendix.
- Convert the volume averaged conservative variables into the interface aver-

aged values by one-dimensional WENO sweeps in $\hat{\mathbf{e}}_1, \hat{\mathbf{e}}_2$, and $\hat{\mathbf{e}}_3$ directions using the weights evaluated or provided in the Appendix and smoothness indicator given in Eq. (39). Ref. to Sections 2.2, 2.3, and 2.4.

- Perform reconstruction of the interface averaged variables to mid-line averages values in the plane of the interface. Perform another reconstruction of the mid-line values in the orthogonal direction to the previous reconstruction in the plane of the interface, to achieve the point value at the mid-point of the interface. Ref. to Section 2.5.
- Calculate flux at the mid-point of each interface by solving the Riemann problem [19].
- Evaluate the source terms at any two mid-points on the opposite faces inside each cell in same orientation across the whole domain. Perform integration in all the directions one by one using point/line-/face-averaged values to yield line-/face-/volume-averaged values of the source term. *Key tip:* If all of the source terms contain ‘ $1/R$ ’ factor, it is advised not to involve radius ($\frac{1}{R}$) term in the tangential averaging, if performed before the radial averaging. While radial averaging, regularized relations are preferred, if the considered points contain $R = 0$ terms. Ref. to Section 2.6.

3. Numerical tests

In this section, several tests on scalar and nonlinear system of equations are performed to analyze the performance of the WENO-C reconstruction scheme. The test cases include scalar advection (1D) on regularly- and irregularly-spaced grids, smooth (1D) and discontinuous inviscid flows (1D/2D) governed by a system of nonlinear equations (Euler equations) on regularly-spaced grids in cylindrical and spherical coordinates. For sake of comparison solely on grounds of the high order reconstruction, time marching in all of the WENO reconstructed 1D test cases is achieved by explicit third order TVD Runge-Kutta scheme

[22, 2]. For 2D test cases, explicit fifth order Runge–Kutta scheme given in [18], is employed to reduce the computation time. Since high order spatial reconstruction with a lower order time marching requires a lower effective value of CFL number (or time step) for domination of spatial errors over temporal errors, the empirical formula to evaluate the time step is given in Eq. (44).

$$\Delta t = C_a \left[\max_{\mathbf{i}} \left(\frac{1}{D} \right) \sum_d \frac{\lambda_{d,\mathbf{i}}}{(\Delta l_{d,\mathbf{i}})^{(ss/tt)}} \right] \quad (44)$$

where C_a is the CFL number, D is the number of spatial dimensions d , while Δl_d and λ_d are the grid length and maximum signal speed inside zone \mathbf{i} in the direction $\hat{\mathbf{e}}_d$. ss and tt are the spatial and temporal orders of convergence respectively.

For a correct initialization in all the tests performed in this paper, the initial condition on the conserved variables is averaged over the corresponding finite volumes $\Delta \mathcal{V}_{\mathbf{i}}$ using seven–point Gaussian quadrature. In multi–dimensions, the averaged values in one dimension are further consecutively averaged in other dimensions using the same quadrature involving line averages. Numerical benchmark test cases for the scalar conservation laws are reported in Section 3.1, while the verification tests for nonlinear systems are presented in Section 3.2. Errors (ϵ_1) are computed using the L_1 discrete norm defined in Eq. (45). In case of a linear system, Q is a generic flow quantity while in case of a nonlinear system of equations, error in density (ρ) is considered.

$$\epsilon_1(Q) = \frac{\sum_{\mathbf{i}} |\bar{Q}_{\mathbf{i}} - \bar{Q}_{\mathbf{i}}^{ref}| \Delta \mathcal{V}_{\mathbf{i}}}{\sum_{\mathbf{i}} \Delta \mathcal{V}_{\mathbf{i}}} \quad (45)$$

where the summation is performed to all of the finite volumes with $\bar{Q}_{\mathbf{i}}^{ref}$ to be the volume average of the reference (or exact) solution and $\Delta \mathcal{V}_{\mathbf{i}}$ is the zone volume.

Finally, the experimental order of convergence (EOC) is computed from Eq.(46).

$$EOC = \frac{\log\left(\frac{\epsilon_1^c(Q)}{\epsilon_1^f(Q)}\right)}{\log\left(\frac{\prod_{d=1}^D N_d^f}{\prod_{d=1}^D N_d^c}\right)} \quad (46)$$

where the superscript c and f refer to the course and fine mesh respectively and N is the number of finite volumes in \hat{e}_d direction.

3.1. Scalar advection tests

As a first benchmark, 1D scalar advection equations Eq. (48) in cylindrical– and spherical–radial coordinates, and Eq. (52) in spherical–meridional coordinates are solved. Two different tests (tests A and B) are performed on a regularly–spaced grid, while test A is also performed on an irregularly–spaced grid. Test A subsumes a monotonic profile while test B is a more stringent test involving a non–monotonic profile. For the irregularly–spaced grid, the grid spacing increases linearly with the radial distance. The summation of all zone lengths is fixed i.e. length of the computational domain and the number of cells (N) is given. A parameter *Ratio* is introduced in Eq. (47) which is an indicator of the level of non–uniformity in computational domain.

$$Ratio = \frac{\text{Grid spacing of any cell in a N-cell uniform grid}}{\text{Grid spacing of the first cell (or the smallest cell) in a N-cell nonuniform grid}} \quad (47)$$

3.1.1. Advection equation in cylindrical– and spherical–radial coordinates

The governing 1D scalar advection equation in cylindrical– and spherical–radial coordinates is formulated in Eq. (48).

$$\frac{\partial Q}{\partial t} + \frac{1}{\xi^m} \frac{\partial}{\partial \xi} (\xi^m Q v) = 0 \quad (48)$$

where the ξ^m is the one–dimensional Jacobian and therefore, $m = 1$ and 2 corresponding to cylindrical– and spherical–radial coordinates respectively.

Velocity v varies linearly with the radial coordinate ξ i.e. $v = \alpha\xi$ and $\alpha = 1$. Eq. (48) admits an exact solution formulated in Eq. (49).

$$Q^{ref}(\xi, t) = e^{-(m+1)\alpha t} Q(\xi e^{-\alpha t}, 0) \quad (49)$$

where $Q(\xi e^{-\alpha t}, 0)$ is the initial condition. For the present case, a Gaussian profile given in Eq. (50) is employed.

$$Q(\xi, 0) = e^{-a^2(\xi-b)^2} \quad (50)$$

where a and b are constants. For the two test cases, $\{a = 10, b = 0\}$ is employed for test A which yields a monotonically decreasing profile and $\{a = 16, b = 1/2\}$ is employed for test B corresponds to a more stringent non-monotonic profile having a maxima at $\xi = 1/2$. The computational domain extends from $\xi = 0$ to $\xi = 2$ consisting of N zones, where boundary conditions include symmetry at the origin ($\xi = 0$) and zero-gradient at $\xi = 2$. Computations are performed until $t = 1$ with a CFL number of 0.9, while the interface flux is computed using Eq. (51).

$$\tilde{F}_{i+\frac{1}{2}} = \frac{1}{2} \left[v_{i+\frac{1}{2}} (Q_{i+1}^- + Q_i^+) - |v_{i+\frac{1}{2}}| (Q_{i+1}^- + Q_i^+) \right] \quad (51)$$

Fig. 3 shows the spatial variation of Q with the radial distance ($\xi = R$) for the two test cases (tests A and B) on a uniform grid in cylindrical- (top) and spherical-radial (bottom) coordinates. For a monotonically decreasing profile (test A), even $N \geq 64$ gives accurate results for both the test cases. However, for test B, $N = 64$ yields slightly lower peaks than the exact solution. When compared with Fig. 2 of [2], a subtly higher peak is observed for test A, since it is a less severe test case. The differences are much more prominent while performing test B. It can be clearly observed that the peaks of $N = 64$ for test B in Fig. 3 are significantly higher than earlier published results [2].

From the experimental order of convergence (EOC) Table 3, it is clear that the WENO-C approaches to the desired fifth order of convergence. The same tests performed in Cartesian coordinates using conventional WENO and present

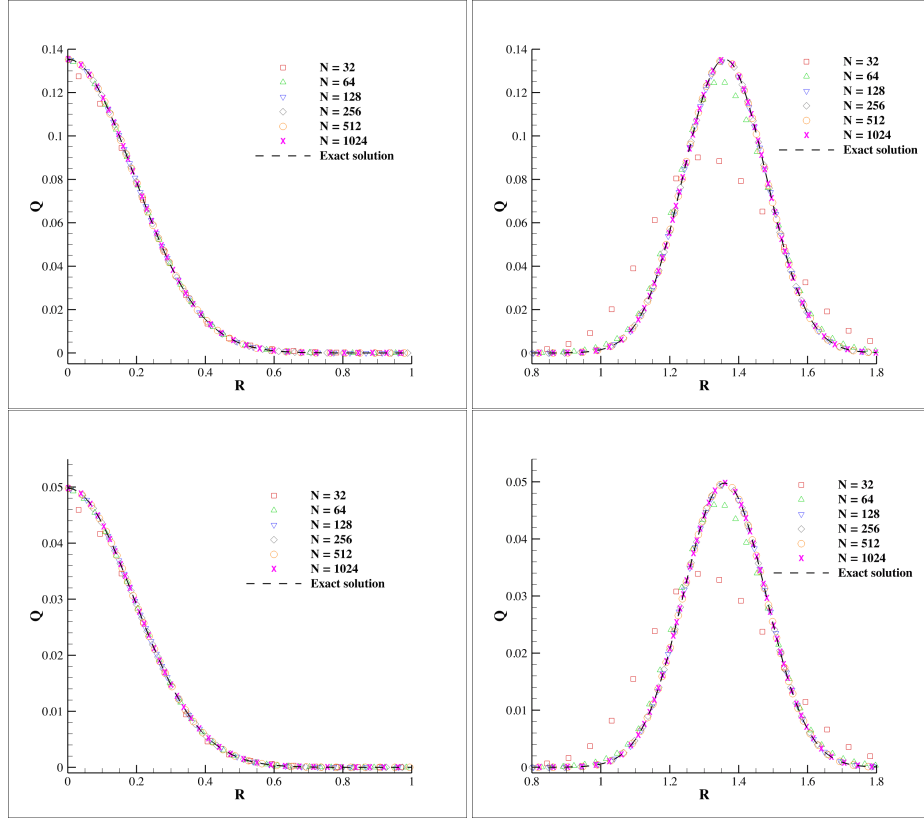


Figure 3: Spatial profiles at $t = 1$ for the radial advection problem in cylindrical– (top) and spherical–radial (bottom) coordinates. Left and right figures correspond to test A $\{a = 10, b = 0\}$ and test B $\{a = 16, b = 1/2\}$ respectively.

WENO–C (both are equivalent) showed same errors and order of convergence (not shown here), and similar behavior as of the cylindrical and spherical grid cases. When compared with Table 1 in [2], present results show a superior performance in terms of accuracy and order of convergence. Modified piecewise parabolic method (PPM₅) approaches fifth order of convergence for test A, however, its order drops down to 2.4 for test B [2].

Fig. 4 illustrates the spatial variation of the conserved variable Q on a non–uniform grid ($N = 16$) while performing test A. It can be clearly inter-

Table 3: L_1 norm errors and experimental order of convergence (EOC) for radial advection test in cylindrical– and spherical–radial coordinates at $t = 1$ for test A $\{a = 10, b = 0\}$ and test B $\{a = 16, b = 1/2\}$.

N	Cylindrical				Spherical			
	Test A		Test B		Test A		Test B	
	$\epsilon_1(Q)$	O_{L_1}	$\epsilon_1(Q)$	O_{L_1}	$\epsilon_1(Q)$	O_{L_1}	$\epsilon_1(Q)$	O_{L_1}
32	9.22E-05	—	1.07E-02	—	1.19E-05	—	3.94E-03	—
64	1.14E-05	3.016	2.10E-03	2.356	1.28E-06	3.208	7.94E-04	2.312
128	4.91E-07	4.537	1.95E-04	3.425	5.28E-08	4.602	7.44E-05	3.415
256	1.94E-08	4.663	9.39E-06	4.378	2.16E-09	4.610	3.58E-06	4.378
512	6.20E-10	4.965	3.14E-07	4.900	6.34E-11	5.093	1.19E-07	4.906
1024	5.81E-11	3.415	1.02E-08	4.941	4.53E-12	3.806	3.88E-09	4.942

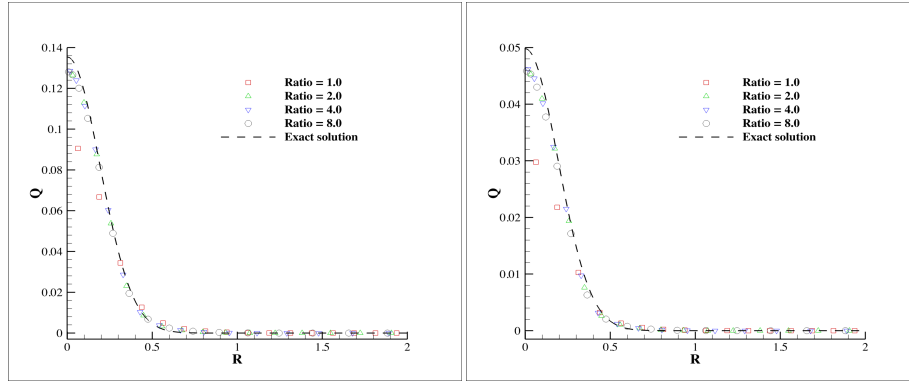


Figure 4: Spatial profiles at $t = 1$ for the radial advection problem (test A: $\{a = 10, b = 0\}$) using $N = 16$ with different values of $Ratio$ (degree of non-uniformity) in cylindrical– (left) / spherical– (right) radial coordinates

Table 4: L_1 norm errors and experimental order of convergence (EOC) for the radial advection problem (test A: $\{a = 10, b = 0\}$) with different values of $Ratio$ (degree of non-uniformity) in cylindrical-/spherical-radial coordinates

N	$Ratio = 1$		$Ratio = 2$		$Ratio = 4$		$Ratio = 8$	
	$\epsilon_1(Q)$	O_{L_1}	$\epsilon_1(Q)$	O_{L_1}	$\epsilon_1(Q)$	O_{L_1}	$\epsilon_1(Q)$	O_{L_1}
Cylindrical								
16	5.54E-04	—	1.85E-04	—	1.70E-04	—	1.80E-04	—
32	9.22E-05	2.587	3.44E-05	2.429	2.78E-05	2.607	3.03E-05	2.573
64	1.14E-05	3.016	1.81E-06	4.247	1.26E-06	4.468	1.39E-06	4.440
128	4.91E-07	4.537	7.89E-08	4.519	5.47E-08	4.523	5.96E-08	4.548
Spherical								
16	5.32E-05	—	2.40E-05	—	2.19E-05	—	2.47E-05	—
32	1.19E-05	2.167	4.48E-06	2.420	3.81E-06	2.523	4.20E-06	2.557
64	1.28E-06	3.208	2.33E-07	4.267	1.72E-07	4.475	1.92E-07	4.449
128	5.28E-08	4.602	9.64E-09	4.594	6.90E-09	4.635	7.57E-09	4.669

puted from the plot that the numerical results approach towards the exact solution with an increase in $Ratio$ (formulated in Eq. 47) i.e. biasing towards the origin. It can be well analyzed from Table 4 that a considerable reduction in errors along with a rapid increase of EOC to the desired order (fifth order) is observed when the grid spacing is biased towards the origin.

3.1.2. Advection equation in spherical-meridional coordinates

The governing 1D scalar advection equation in spherical-meridional coordinates is given in Eq. (52).

$$\frac{\partial Q}{\partial t} + \frac{1}{\sin\theta} \frac{\partial}{\partial\theta}(\sin\theta Q v) = 0 \quad (52)$$

where the velocity v varies linearly with the θ coordinate i.e. $v = \alpha\theta$ and

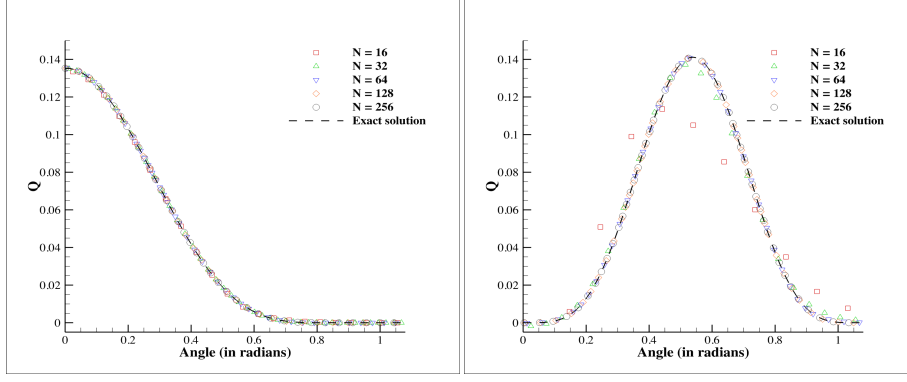


Figure 5: Spatial profiles at $t = 1$ for the scalar advection problem in spherical-meridional coordinates with different mesh points. Left and right subfigures refer to test A $\{a = 10, b = 0\}$ and B $\{a = 15, b = \pi/a\}$ respectively.

$\alpha = 1$. The exact solution of Eq. (52) is formulated in Eq. (53).

$$Q^{ref}(\xi, t) = e^{-\alpha t} \frac{\sin(e^{-\alpha t} \theta)}{\sin \theta} Q(e^{-\alpha t} \theta, 0) \quad (53)$$

A 1D computational grid spanning the interval $\theta \in [0, \pi/2]$ is divided into N zones. Initial condition ($t = 0$) for the problem is given in Eq. (54).

$$Q(\theta, 0) = \begin{cases} \left[\frac{1 + \cos(a(\theta - b))}{2} \right]^2 & |\theta - b| < \frac{\pi}{a} \\ 0 & \text{otherwise} \end{cases} \quad (54)$$

where a and b are constants. Two different tests are performed namely, test A with $\{a = 10, b = 0\}$ yielding a monotonically decreasing profile and a more stringent test B $\{a = 16, b = \pi/a\}$ resulting in a non-monotonic profile having a maxima at $\theta = \pi/a$. The computational domain extends from $\theta = 0$ to $\theta = \pi/2$, where the boundary conditions include symmetry at the origin ($\theta = 0$) and zero-derivative at $\theta = \pi/2$. Computations are performed till $t = 1$ with a CFL number of 0.9, while the interface flux is computed using Eq. (51).

Fig. 5 shows the spatial variation of the conserved variable Q with the angle θ for both of the test cases. For test A, even $N = 16$ give accurate results, while for test B, $N \geq 32$ provide a good approximation of the exact solution. Table

Table 5: L_1 norm errors and experimental order of convergence (EOC) for scalar advection test in spherical–meridional coordinates at $t = 1$ for test A $\{a = 10, b = 0\}$ and test B $\{a = 16, b = \pi/a\}$ respectively.

N	Test A		Test B	
	$\epsilon_1(Q)$	O_{L_1}	$\epsilon_1(Q)$	O_{L_1}
32	1.71E-04	—	1.57E-03	—
64	1.99E-05	3.103	2.11E-04	2.894
128	7.10E-07	4.808	1.62E-05	3.699
256	2.25E-08	4.978	4.81E-07	5.078

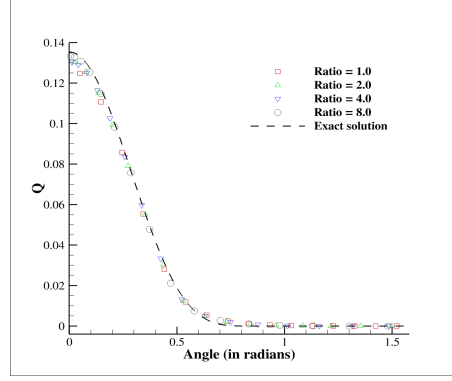


Figure 6: Spatial profiles at $t = 1$ for the scalar advection problem (test A: $\{a = 10, b = 0\}$) using $N = 16$ with different values of $Ratio$ (degree of non–uniformity) in spherical–meridional coordinates.

5 illustrates the achievement of the desired fifth order of convergence for both the test cases. When the results obtained by the present scheme are compared with the schemes present in Table 2 of [2], it is realized that WENO–C shows a superior performance. For the non–uniform mesh case, fifth order of convergence is still preserved with a rapid achievement of fifth order of convergence, as summarized in Table 6. Moreover, Fig. 6 shows that mesh biasing provides results closer to the exact solution with a significant reduction in the errors with a same number of cells.

Table 6: L_1 norm errors and experimental order of convergence (EOC) for the scalar advection problem (test A: $\{a = 10, b = 0\}$) with different values of $Ratio$ (degree of non-uniformity) in spherical-meridional coordinates

N	$Ratio = 1$		$Ratio = 2$		$Ratio = 4$		$Ratio = 8$	
	$\epsilon_1(Q)$	O_{L_1}	$\epsilon_1(Q)$	O_{L_1}	$\epsilon_1(Q)$	O_{L_1}	$\epsilon_1(Q)$	O_{L_1}
16	7.43E-04	—	4.27E-04	—	4.61E-04	—	5.05E-04	—
32	1.71E-04	2.120	9.18E-05	2.217	1.01E-04	2.195	1.16E-04	2.128
64	1.99E-05	3.103	8.33E-06	3.463	9.13E-06	3.465	1.07E-05	3.438
128	7.10E-07	4.808	2.45E-07	5.085	2.72E-07	5.069	3.24E-07	5.040

3.2. Euler equations based tests

The present reconstruction scheme is now tested for more challenging test cases involving nonlinear systems of equations i.e. Euler equations. Although primitive variable reconstruction is preferred in the past due to achieving well-behaved results involved, for the case of curvilinear coordinates, involvement of the higher order derivatives in the extraction of the primitive variables causes spurious oscillations [2]. Therefore, we restrict our work to the reconstruction of the conserved variables instead of computationally expensive and intricate primitive variable reconstruction. Maximum characteristic speed is employed to evaluate the time step from Eq. (44). Several tests are performed in cylindrical and spherical coordinates to investigate the essentially non-oscillatory property of WENO-C in the discontinuous flows and the convex combination property in the smooth flows.

3.2.1. Isothermal radial wind problem

The isothermal 1D radial wind problem is performed to analyze the deviations of spatial reconstruction schemes near the origin in curvilinear coordinates [2]. The general form of Euler equation in 1D Cartesian / cylindrical- /

spherical–radial coordinates can be written in the form of Eq. (55).

$$\frac{\partial}{\partial t} \begin{pmatrix} \rho \\ \rho v \\ E \end{pmatrix} + \frac{1}{\xi^m} \frac{\partial}{\partial r} \begin{pmatrix} \rho v \xi^m \\ (\rho v^2 + p) \xi^m \\ (E + p) v \xi^m \end{pmatrix} = \begin{pmatrix} 0 \\ mp/\xi \\ 0 \end{pmatrix} \quad (55)$$

where ρ is the mass density, v is the radial velocity, p is the pressure, E is the total energy, and $m = 0, 1$, and 2 for Cartesian, cylindrical–, and spherical–radial coordinates respectively. For an isothermal flow, the energy equation is discarded whereas Eq. (56) serves as the adiabatic equation of state (EOS).

$$E = \frac{p}{\gamma - 1} + \frac{1}{2} \rho v^2 \quad (56)$$

where $\gamma = 5/3$ is assumed for this case. At $\xi = 0$ axisymmetric boundary conditions apply while at the outer edge density, pressure and scaled velocity ($v/\bar{\xi}$) have zero gradient. The initial conditions are provided in Eq. (57) and the interface flux is evaluated with Lax-Friedrichs scheme with local speed estimate [23].

$$\rho(\xi, 0) = 1; \quad v(\xi, 0) = 100\xi; \quad p(\xi, 0) = 1/\gamma \quad (57)$$

The computational domain spanning $0 \leq \xi \leq 2$ is divided into $N = 100$ points. The spatial profiles of density (ρ ; left) and scaled velocity ($v/\bar{\xi}$; right) are plotted in Fig. 7 after one integration step $\Delta t = 7 \times 10^{-5}$ for the case of cylindrical and spherical grid. Here, $\bar{\xi}$ represents the location of the centroid as discussed in section 2.4. Comparing it with the previously published results [2, 24], it is noteworthy that the density and scaled velocity remain linear and no signs of deviations are observed near the origin.

3.2.2. Acoustic wave propagation

A smooth problem involving nonlinear system of 1D gas dynamical equations is solved to testify the fifth order of convergence. The original problem introduced by Johnsen and Colonius [25] is adapted to cylindrical and spherical

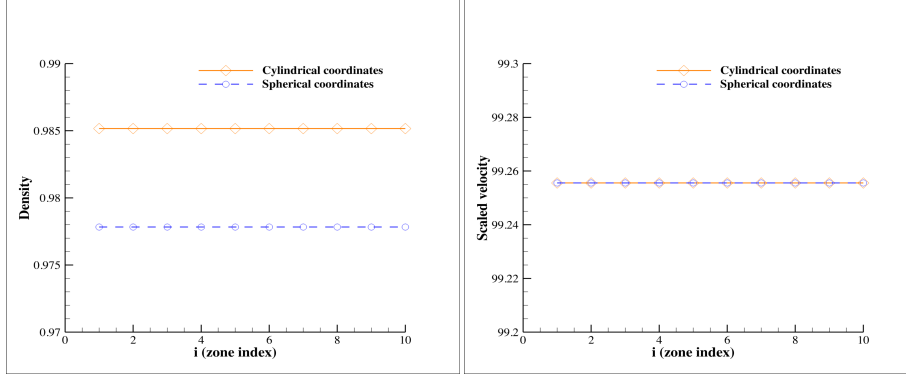


Figure 7: Spatial profiles of density (ρ ; left) and scaled radial velocity ($v/\bar{\xi}$; right) for the isothermal radial wind problem [24, 2] with constant density after one timestep in cylindrical–(orange, diamonds) and spherical–radial (blue, circles) coordinates. Only the region close to the origin shown.

coordinates [26]. The governing equations and initial conditions for this test are provided in Eqs. (55, 56) and (58) respectively.

$$\rho(r, 0) = 1 + \varepsilon f(r), \quad u(r, 0) = 0, \quad p(r, 0) = 1/\gamma + \varepsilon f(r) \quad (58)$$

with the perturbation,

$$f(r) = \begin{cases} \frac{\sin^4(5\pi r)}{r} & \text{if } 0.4 \leq r \leq 0.6 \\ 0 & \text{otherwise} \end{cases} \quad (59)$$

where $\gamma = 1.4$. A sufficiently small ε ($\varepsilon = 10^{-4}$) yields a smooth solution. The interface flux is evaluated using Lax–Friedrichs scheme with local speed estimate [23] with a CFL number of 0.3.

The initial perturbation splits into two acoustic waves travelling in opposite directions. The final time ($t = 0.3$) is set such that the waves remain in the domain and the problem is free from the boundary effects. The computational domain of unity length is uniformly divided into different zones N i.e. $N = 16, 32, 64, 128, 256$. Although an exact solution known up to $O(\varepsilon^2)$ is known, the solution on the finest mesh $N = 1024$ is considered to be the reference. Error in density is evaluated from Eq. (45). Fig. 8 illustrate the spatial variation of

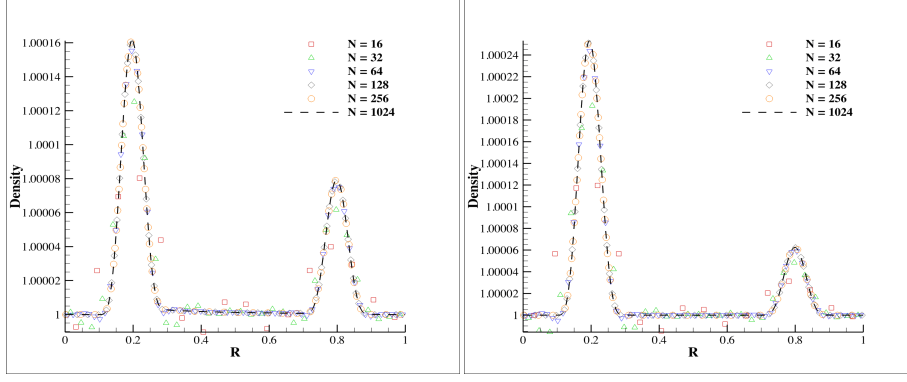


Figure 8: Spatial profiles of density (ρ) acoustic wave propagation problem [25, 26] at time $t = 0.3$ in cylindrical– (left) and spherical–radial (right) coordinates.

Table 7: L_1 norm errors and experimental order of convergence (EOC) for acoustic wave propagation test in cylindrical– and spherical–radial coordinates at $t = 0.3$.

N	Cylindrical		Spherical	
	$\epsilon_1(Q)$	O_{L_1}	$\epsilon_1(Q)$	O_{L_1}
16	1.01E-05	—	7.98E-06	—
32	4.91E-06	1.036	3.90E-06	1.033
64	6.74E-07	2.865	5.40E-07	2.852
128	3.24E-08	4.380	2.59E-08	4.383
256	1.27E-09	4.670	1.01E-09	4.675

density at $t = 1$ inside the domain in cylindrical– (left) and spherical–radial (right) coordinates. The location of the peaks is same, however, the difference in the height of the peaks occurs due to the different one–dimensional Jacobians for both the cases. From Table 7, it clear that the scheme approaches the desired fifth order of convergence (EOC) for both the cases.

3.2.3. Sedov explosion test

Sedov explosion test is performed to test the code’s ability to deal with strong shocks and non–planar symmetry [27]. The problem involves a self–similar evolution of a cylindrical / spherical blastwave from a localized (delta–function)

initial pressure perturbation in an otherwise homogeneous medium. Governing equations for this problem are the same as given in Eq. (55) earlier. For the code initialization, dimensionless energy $\epsilon = 1$ is deposited into a small region of radius δr , which is 3 times the cell size at the center. Inside this region, the dimensionless pressure P'_0 is given in Eq. (60).

$$P'_0 = \frac{3(\gamma - 1)\epsilon}{(m + 2)\pi\delta r^{(m+1)}} \quad (60)$$

where $\gamma = 1.4$ and $m = 1, 2$ for cylindrical and spherical geometries respectively. Reflecting boundary condition is employed at the center ($R = 0$), while the outflow boundary ($R = 1$) condition is irrelevant for this problem. The initial velocity and density inside the domain are 0 and 1 respectively and the initial pressure everywhere except the kernel is 10^{-5} . Due to the reflecting boundary condition at the center, the high pressure region is made up of 6 cells, i.e., 3 ghost cells and 3 interior cells. The CFL number is 0.1 as the source term is very stiff and the final result time is $t = 0.05$. In a self-similar blastwave that develops, the analytical results of the variation near the grid, behind the shock, and shock location are provided in [27].

Fig. 9 shows the variation of density, velocity, and pressure with radius on a uniform grid ($N = 100, 200$) in 1D cylindrical- and spherical-radial coordinates. The analytical values of the shock locations are specified as 0.2236 and 0.3017 for cylindrical and spherical geometries respectively. Also, the peaks values of the pressure, velocity, and density show similar behavior as given in [26], but the locations of the shocks are different due to different ϵ and final time values.

3.2.4. SOD test

SOD test [28] is considered in 1D cylindrical- and spherical-radial (r) and 2D cylindrical ($r - \theta$) coordinates. For 1D cases, the governing equation is given in Eq. (55), while the governing equation in cylindrical ($r - \theta$) coordinates is

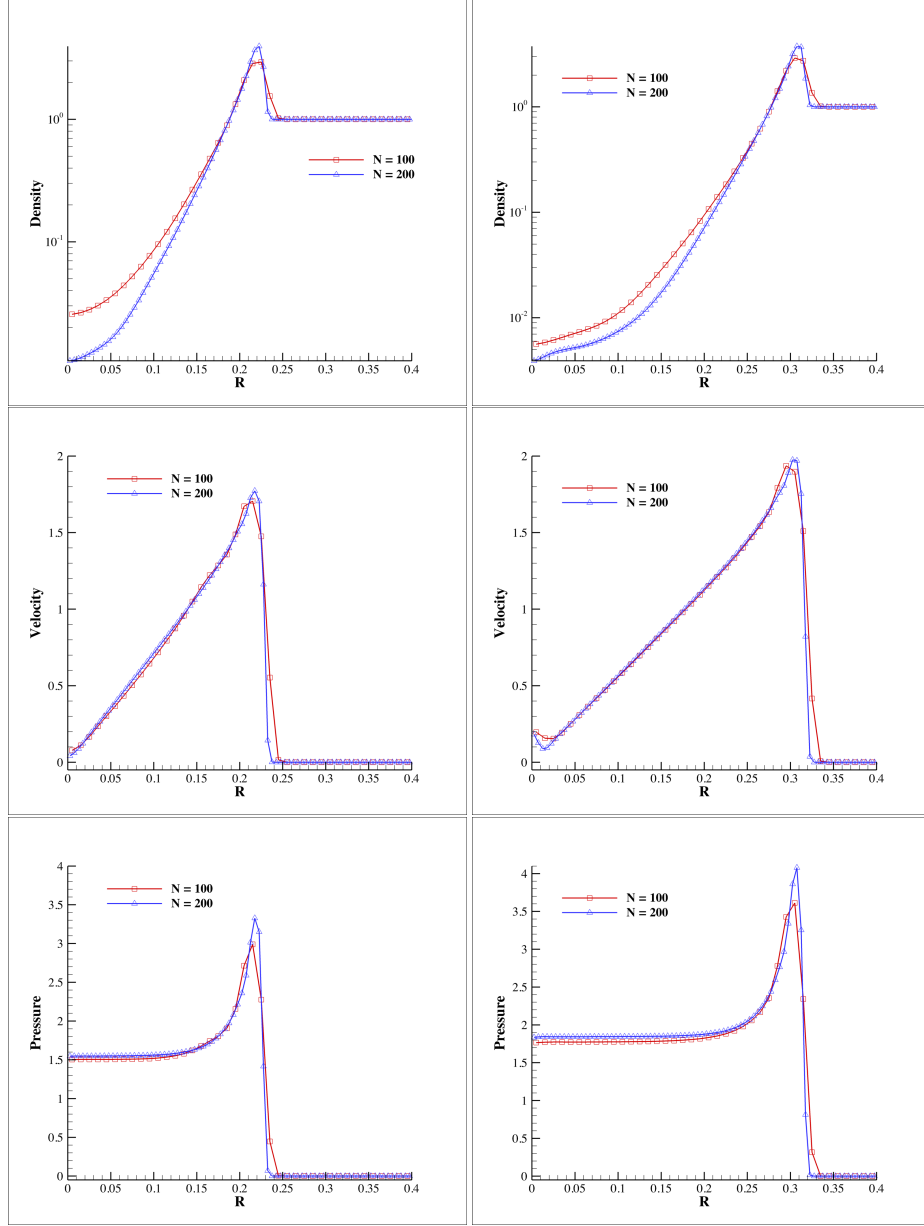


Figure 9: Variation of density (first row), velocity (middle row), and pressure (third row) with the radius for cylindrical– (left column) and spherical–radial (right column) coordinates for the Sedov explosion test [27, 26]. Domain is restricted to $R = 0.4$ for the sake of clarity.

given in Eq. (61).

$$\frac{\partial}{\partial t} \begin{pmatrix} \rho \\ \rho v_r \\ \rho v_\theta \\ \rho e \end{pmatrix} + \frac{1}{r} \frac{\partial}{\partial r} \begin{pmatrix} \rho v_r r \\ (\rho v_r^2 + p)r \\ \rho v_r v_\theta r \\ (\rho e + p)v_r r \end{pmatrix} + \frac{1}{r} \frac{\partial}{\partial \theta} \begin{pmatrix} \rho v_\theta \\ \rho v_r v_\theta \\ \rho v_\theta^2 + p \\ (\rho e + p)v_\theta \end{pmatrix} = \begin{pmatrix} 0 \\ (p + \rho v_\theta^2)/r \\ -\rho v_r v_\theta/r \\ 0 \end{pmatrix} \quad (61)$$

where terms $(\rho v_\theta^2)/r$ and $(\rho v_r v_\theta)/r$ are related to the centrifugal and Coriolis forces respectively. The interface flux in this problem is evaluated with HLL Riemann solver [29]. The initial condition consists of two uniform regions inside the domain separated by a diaphragm at $r = 0.5$. The left and right states are respectively provided in Eq. (62).

$$\begin{pmatrix} \rho \\ v_r \\ v_\theta \\ p \end{pmatrix}_L = \begin{pmatrix} 1 \\ 0 \\ 0 \\ 1 \end{pmatrix}; \quad \begin{pmatrix} \rho \\ v_r \\ v_\theta \\ p \end{pmatrix}_R = \begin{pmatrix} 0.125 \\ 0 \\ 0 \\ 0.1 \end{pmatrix} \quad (62)$$

The computational domain ($0 \leq r \leq 1$) for 1D tests is uniformly divided in $N = 100,500$ zones, while for the 2D test case the domain ($0 \leq r \leq 1$, $0 \leq \theta \leq \pi/2$) is uniformly divided into 100×100 zones in the corresponding directions. The boundary conditions for 1D cases are irrelevant, however, for 2D case are symmetric at $r = 0$ (except radial velocity which is antisymmetric) with outflow boundary condition applied to other boundaries namely $r = 1$, $\theta = 0$, and $\theta = \pi/2$. The computation is performed till $t = 0.2$ with a CFL number of 0.3. For first order and second order (MUSCL [30]) spatial reconstruction, Euler time marching and Maccormack (predictor–corrector) schemes [31], are respectively employed.

Figs. 10 shows the spatial profiles of density, velocity, and pressure for the case of SOD test in 1D/2D cylindrical coordinates (left) and 1D spherical–radial coordinates. WENO–C performs better than first order and second order (MUSCL [30]) reconstruction techniques. The 2D test results exactly overlap

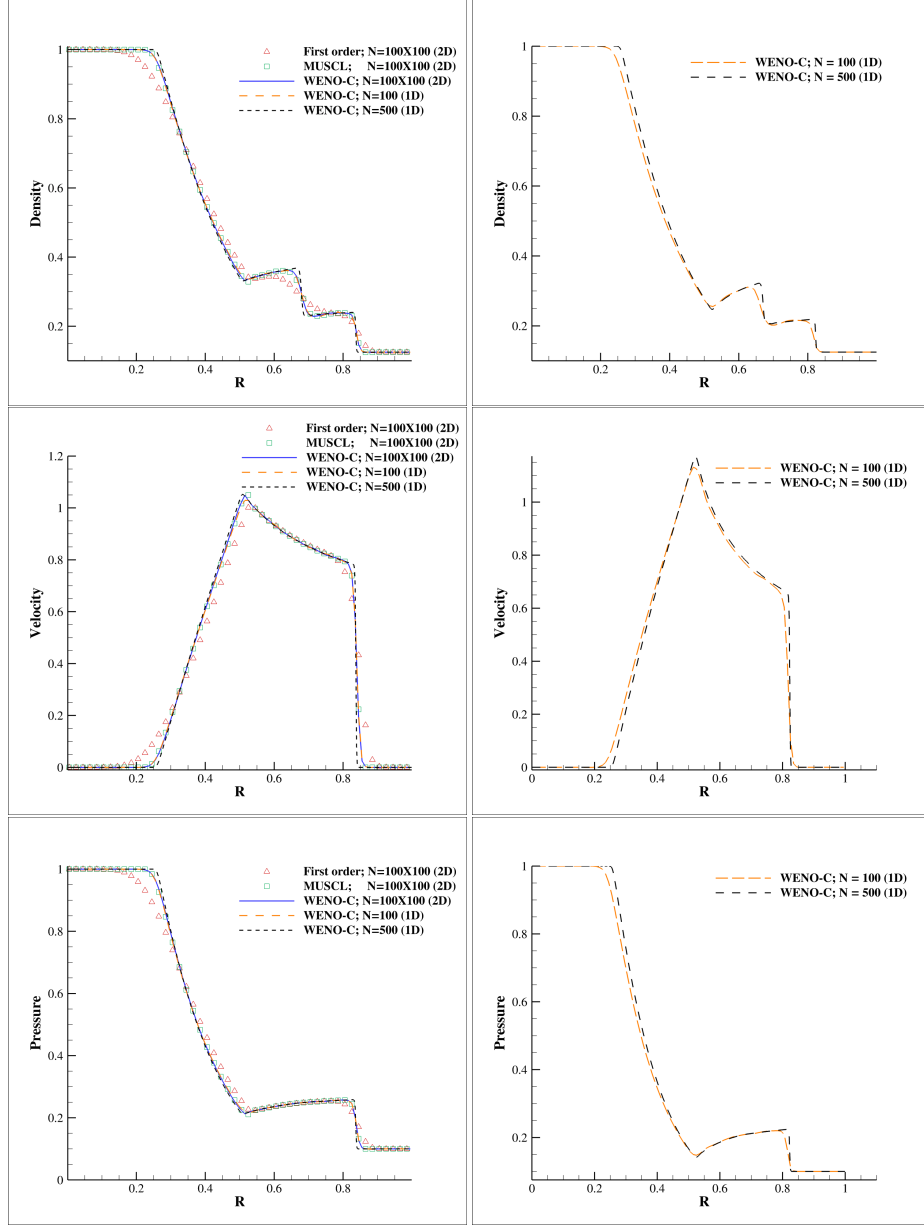


Figure 10: Variation of density (first row), velocity (middle row), and pressure (third row) with the radius at $t = 0.2$ for cylindrical– (left column) and spherical–radial (right column) coordinates for the modified SOD test [28, 26].

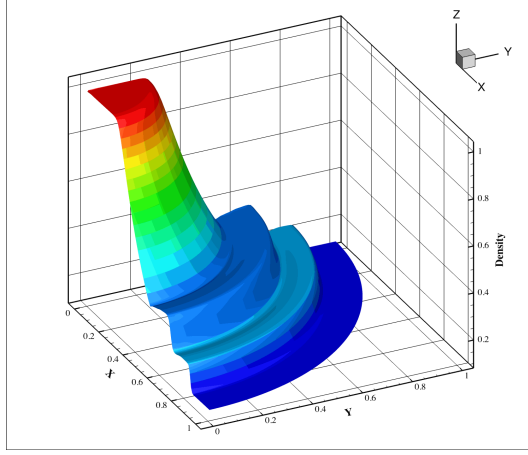


Figure 11: Variation of density with the radius at $t = 0.2$ for cylindrical $(r - \theta)$ coordinates in the Cartesian plane for the modified SOD test [28, 26].

with the 1D test results in cylindrical coordinates. Fig. 11 shows the spatial variation of the density in the 2D Cartesian plane at time $t = 0.2$. When compared with the results presented in [26], it is clear that WENO-C yields similar results to the fifth order finite difference WENO but the results in the present work are less oscillatory and are well-behaved than the latter.

3.2.5. Modified 2D Riemann problem in cylindrical $(R-z)$ coordinates

The final test of the present scheme involves a 2D Riemann problem in cylindrical $(R - z)$ coordinates. The problem corresponds to the configuration 12 of [32] involving 2 contact discontinuity and 2 shocks as the initial condition, resulting in the formation of a self-similar structure propagating towards the low density-low pressure region. To make the problem symmetric about the origin, the original problem [32] is rotated by an angle of 45 degrees in the clockwise direction. The modified 2D Riemann problem is illustrated in Fig. 12. The governing equations are provided in Eq. (63).

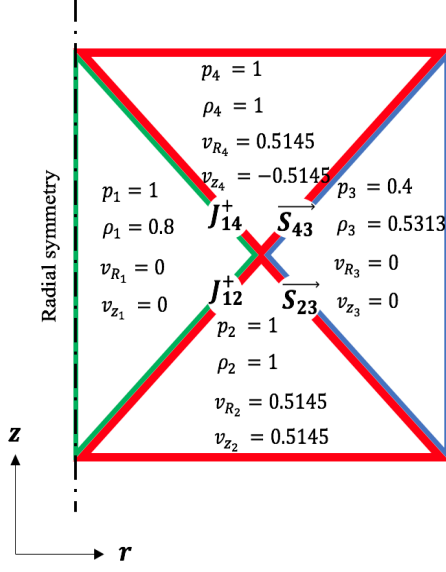


Figure 12: A schematic of modified 2D Riemann problem in cylindrical $(r - z)$ coordinates.

$$\frac{\partial}{\partial t} \begin{pmatrix} \rho \\ \rho v_R \\ \rho v_z \\ \rho e \end{pmatrix} + \frac{1}{R} \frac{\partial}{\partial R} \begin{pmatrix} \rho v_R R \\ (\rho v_R^2 + p) R \\ \rho v_R v_z R \\ (\rho e + p) v_R R \end{pmatrix} + \frac{\partial}{\partial z} \begin{pmatrix} \rho v_z \\ \rho v_R v_z \\ \rho v_z^2 + p \\ (\rho e + p) v_z \end{pmatrix} = \begin{pmatrix} 0 \\ p/R \\ 0 \\ 0 \end{pmatrix} \quad (63)$$

The computations are performed with a CFL number of 0.5 until $t = 0.2$ on a $(r, z) = [0, 1] \times [0, 1]$ domain divided into 500×500 zones. The boundary conditions include symmetry at the center (except for the antisymmetric radial velocity) and outflow elsewhere. For first order and second order (MUSCL [30]) spatial reconstruction, Euler time marching and Maccormack (predictor–corrector) schemes [31], are respectively employed. From Fig. 13, it is clear that the WENO–C provides rich structures, especially in the contact–contact region (region 1). The small scale structures are much clear and rich in the present reconstruction scheme, when compared with the second order MUSCL reconstruction. Structures are highly smeared for the case of first order reconstruction.

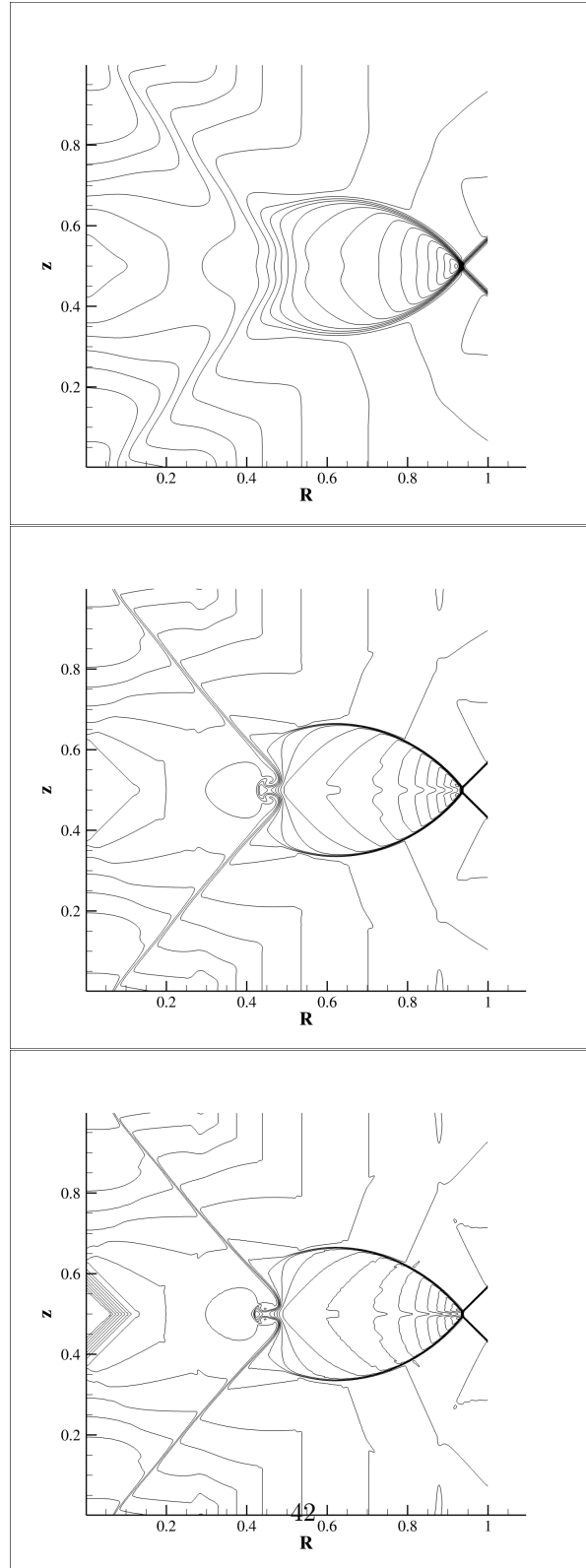


Figure 13: Density contours with different reconstruction techniques (first order (top), second order MUSCL [30] (middle), and WENO-C (bottom)) at $t = 0.2$ for the modified Riemann problem in cylindrical $(r - z)$ coordinates

4. Conclusions

The fifth order finite volume WENO reconstruction scheme provides a more general framework in the orthogonally–curvilinear coordinates to achieve high order spatial accuracy with minimal computational cost. Linear weights, non-linear weights, weights for mid–point interpolation and source term integration are derived for the standard grids. This simple and more physical scheme of reconstruction in original coordinates can be applied to both regularly– and irregularly–spaced grids. A grid independent smoothness indicator is derived from the basic definition. The analytical values for the uniform Cartesian grid and even cylindrical– and spherical–radial grids for $R \rightarrow \infty$ conform to the original WENO scheme introduced by Jiang and Shu. 1D Scalar advection tests are performed in curvilinear coordinates on regularly– and irregularly–spaced grids followed by several smooth and discontinuous flow test cases in 1D spherical coordinates and 1D/2D cylindrical coordinates testify the high order accuracy and ENO property of the scheme. For a multi–dimensional test case, external values are considered to integrate the source term, while for 1D test cases, mid–point values are reconstructed for the source term integration. As a final note, it is emphasized that the present scheme can be extended to arbitrary order of accuracy and different methods of reconstruction in multi–dimensions.

Appendix A. WENO-C reconstruction weights

Appendix A.1. Cartesian coordinates

Weights for the uniform grid Cartesian coordinates is provided for the sake of completeness the present scheme and ease of understanding of the reader for in the next subsections.

Appendix A.1.1. Linear weights

In the case of Cartesian coordinates (x, y, z) , the linear weights are obtained by putting $m = 0$ in Eq. (26) and then inverting the β –matrix in Eq. (24).

- Positive (right) weights:

$$\begin{aligned} S_0^{3+}(i-2, i-1, i) &:: (w_{i,0,-2}^{3+}, w_{i,0,-1}^{3+}, w_{i,0,0}^{3+}) = \left(\frac{1}{3}, -\frac{7}{6}, \frac{11}{6} \right) \\ S_1^{3+}(i-1, i, i+1) &:: (w_{i,1,-1}^{3+}, w_{i,1,0}^{3+}, w_{i,1,+1}^{3+}) = \left(-\frac{1}{6}, \frac{5}{6}, \frac{1}{3} \right) \\ S_2^{3+}(i, i+1, i+2) &:: (w_{i,2,0}^{3+}, w_{i,2,+1}^{3+}, w_{i,2,+2}^{3+}) = \left(\frac{1}{3}, \frac{5}{6}, -\frac{1}{6} \right) \end{aligned}$$

- Middle weights:

$$\begin{aligned} S_0^{3M}(i-2, i-1, i) &:: (w_{i,0,-2}^{3M}, w_{i,0,-1}^{3M}, w_{i,0,0}^{3M}) = \left(-\frac{1}{24}, \frac{1}{12}, \frac{23}{24} \right) \\ S_1^{3M}(i-1, i, i+1) &:: (w_{i,1,-1}^{3M}, w_{i,1,0}^{3M}, w_{i,1,+1}^{3M}) = \left(-\frac{1}{24}, \frac{13}{12}, -\frac{1}{24} \right) \\ S_2^{3M}(i, i+1, i+2) &:: (w_{i,2,0}^{3M}, w_{i,2,+1}^{3M}, w_{i,2,+2}^{3M}) = \left(\frac{23}{24}, \frac{1}{12}, -\frac{1}{24} \right) \end{aligned}$$

- Negative (left) weights:

$$\begin{aligned} S_0^{3-}(i-2, i-1, i) &:: (w_{i,0,-2}^{3-}, w_{i,0,-1}^{3-}, w_{i,0,0}^{3-}) = \left(-\frac{1}{6}, \frac{5}{6}, \frac{1}{3} \right) \\ S_1^{3-}(i-1, i, i+1) &:: (w_{i,1,-1}^{3-}, w_{i,1,0}^{3-}, w_{i,1,+1}^{3-}) = \left(\frac{1}{3}, \frac{5}{6}, -\frac{1}{6} \right) \\ S_2^{3-}(i, i+1, i+2) &:: (w_{i,2,0}^{3-}, w_{i,2,+1}^{3-}, w_{i,2,+2}^{3-}) = \left(\frac{11}{6}, -\frac{7}{6}, \frac{1}{3} \right) \end{aligned}$$

Appendix A.1.2. Fifth order interpolation weights

- Positive (right) weights:

$$S_0^{5+} :: (w_{i,0,-2}^{5+}, w_{i,0,-1}^{5+}, w_{i,0,0}^{5+}, w_{i,0,+1}^{5+}, w_{i,0,+2}^{5+}) = \left(\frac{1}{30}, -\frac{13}{60}, \frac{47}{60}, \frac{9}{20}, -\frac{1}{20} \right)$$

- Middle weights:

$$S_0^{5M} :: (w_{i,0,-2}^{5M}, w_{i,0,-1}^{5M}, w_{i,0,0}^{5M}, w_{i,0,+1}^{5M}, w_{i,0,+2}^{5M}) = \left(\frac{3}{640}, -\frac{29}{480}, \frac{1067}{960}, -\frac{29}{480}, \frac{3}{640} \right)$$

- Negative (left) weights:

$$S_0^{5-} :: (w_{i,0,-2}^{5-}, w_{i,0,-1}^{5-}, w_{i,0,0}^{5-}, w_{i,0,+1}^{5-}, w_{i,0,+2}^{5-}) = \left(-\frac{1}{20}, \frac{9}{20}, \frac{47}{60}, -\frac{13}{60}, \frac{1}{30} \right)$$

Appendix A.1.3. Optimal weights

The linear weights in the Cartesian coordinates in (x, y, z) coordinates are a constant, thus, the optimal weight is also a constant. Moreover, they are mirror-symmetric for the case of positive and negative weights as shown below.

- Positive (right) weights:: $(C_{i,0}^+, C_{i,1}^+, C_{i,2}^+) = \left(\frac{1}{10}, \frac{3}{5}, \frac{3}{10} \right)$

- Middle weights:: $(C_{i,0}^M, C_{i,1}^M, C_{i,2}^M) = \left(-\frac{9}{80}, \frac{49}{40}, -\frac{9}{80}\right)$
- Negative (left) weights:: $(C_{i,0}^-, C_{i,1}^-, C_{i,2}^-) = \left(\frac{3}{10}, \frac{3}{5}, \frac{1}{10}\right)$

Appendix A.1.4. Weights for interface value integration

In this case the one-dimensional Jacobian is unity, therefore, the weights for flux integration and source term integration are the same. The weights for interface value integration to yield line-/face- averaged flux with different integration points are provided as follows:

- Fifth order (all middle values):: $(w_{i,-2}^M, w_{i,-1}^M, w_{i,0}^M, w_{i,+1}^M, w_{i,+2}^M) = \left(-\frac{17}{5760}, \frac{77}{1440}, \frac{863}{960}, \frac{77}{1440}, -\frac{17}{5760}\right)$
- Sixth order (all interface values):: $(w_{i,-5/2}^+, w_{i,-3/2}^+, w_{i,-1/2}^+, w_{i,+1/2}^-, w_{i,+3/2}^-, w_{i,+5/2}^-) = \left(\frac{11}{1440}, -\frac{31}{480}, \frac{401}{720}, \frac{401}{720}, -\frac{31}{480}, \frac{11}{1440}\right)$

Appendix A.1.5. Weights for source term integration

In this case, since the one-dimensional Jacobian is unity weights for flux integration and source term integration are the same. For 1D case, 3 point based Simpson quadrature can be performed which yields the same fifth order accuracy.

- Three point based Simpson quadrature (2 interface, 1 middle values):: $(w_{i,-1/2}^+, w_{i,0}^M, w_{i,+1/2}^-) = \left(\frac{1}{6}, \frac{2}{3}, \frac{1}{6}\right)$
- Fifth order (all middle values):: Ref. to Appendix A.1.4
- Sixth order (all interface values):: Ref. to Appendix A.1.4

Appendix A.2. Cylindrical coordinates

Appendix A.2.1. Linear weights

In the case of cylindrical coordinates (θ, z) , the linear weights are obtained by putting $m = 0$ in Eq. (26) and then inverting the β -matrix in Eq. (24). For this case, the weights are the same as in the Cartesian coordinates given in the

Appendix A.1.1. However, for the case of radial coordinate (R), $m = 1$ is used and the weights are given below, where $i = \frac{R_{i+\frac{1}{2}}}{\Delta R}$ is independent of the grid spacing and depends only on the index number of the grid. In the vanishing curvature ($R \rightarrow \infty$ and therefore $i \rightarrow \infty$), the linear weights of the conventional WENO reconstruction in Cartesian coordinates can be recovered.

- Positive (right) weights:

$$\begin{aligned} S_0^+(i-2, i-1, i) :: \quad (w_{i,0,-2}^{3+}, w_{i,0,-1}^{3+}, w_{i,0,0}^{3+}) &= \left(\frac{(-5+2i)(4-9i+4i^2)}{12(-3+2i)(1-3i+i^2)}, \frac{-23+45i-14i^2}{12(1-3i+i^2)}, \frac{(-1+2i)(85-90i+22i^2)}{12(-3+2i)(1-3i+i^2)} \right) \\ S_1^+(i-1, i, i+1) :: \quad (w_{i,1,-1}^{3+}, w_{i,1,0}^{3+}, w_{i,1,+1}^{3+}) &= \left(-\frac{(-3+2i)(-1+2i^2)}{12(-1+2i)(-1-i+i^2)}, \frac{11+9i-10i^2}{12(1+i-i^2)}, -\frac{-4+i+14i^2-8i^3}{12(1-i-3i^2+2i^3)} \right) \\ S_2^+(i, i+1, i+2) :: \quad (w_{i,2,0}^{3+}, w_{i,2,+1}^{3+}, w_{i,2,+2}^{3+}) &= \left(\frac{(-1+2i)(4+9i+4i^2)}{12(1+2i)(-1+i+i^2)}, \frac{-11+9i+10i^2}{12(-1+i+i^2)}, -\frac{(3+2i)(-1+2i^2)}{12(1+2i)(-1+i+i^2)} \right) \end{aligned}$$

- Middle weights:

$$\begin{aligned} S_0^{3M}(i-2, i-1, i) :: \quad (w_{i,0,-2}^{3M}, w_{i,0,-1}^{3M}, w_{i,0,0}^{3M}) &= \left(\frac{5+3i-7i^2+2i^3}{72-264i+216i^2-48i^3}, \frac{-4-i+i^2}{12(1-3i+i^2)}, \frac{(-1+2i)(91-95i+23i^2)}{24(-3+2i)(1-3i+i^2)} \right) \\ S_1^{3M}(i-1, i, i+1) :: \quad (w_{i,1,-1}^{3M}, w_{i,1,0}^{3M}, w_{i,1,+1}^{3M}) &= \left(-\frac{3-2i}{24+48i}, \frac{13}{12}, \frac{1+2i}{24-48i} \right) \\ S_2^{3M}(i, i+1, i+2) :: \quad (w_{i,2,0}^{3M}, w_{i,2,+1}^{3M}, w_{i,2,+2}^{3M}) &= \left(\frac{(-1+2i)(19+49i+23i^2)}{24(1+2i)(-1+i+i^2)}, \frac{-4-i+i^2}{12(-1+i+i^2)}, -\frac{(3+2i)(-1-i+i^2)}{24(1+2i)(-1+i+i^2)} \right) \end{aligned}$$

- Negative (left) weights:

$$\begin{aligned} S_0^-(i-2, i-1, i) :: \quad (w_{i,0,-2}^{3-}, w_{i,0,-1}^{3-}, w_{i,0,0}^{3-}) &= \left(-\frac{(-5+2i)(1-4i+2i^2)}{12(-3+2i)(1-3i+i^2)}, \frac{8-29i+10i^2}{12(1-3i+i^2)}, \frac{(-1+2i)(17-17i+4i^2)}{12(-3+2i)(1-3i+i^2)} \right) \\ S_1^-(i-1, i, i+1) :: \quad (w_{i,1,-1}^{3-}, w_{i,1,0}^{3-}, w_{i,1,+1}^{3-}) &= \left(\frac{(-3+2i)(-1+i+4i^2)}{12(-1+2i)(-1-i+i^2)}, \frac{10+11i-10i^2}{12(1+i-i^2)}, \frac{-1+2i+6i^2-4i^3}{12(1-i-3i^2+2i^3)} \right) \\ S_2^-(i, i+1, i+2) :: \quad (w_{i,2,0}^{3-}, w_{i,2,+1}^{3-}, w_{i,2,+2}^{3-}) &= \left(\frac{(-1+2i)(17+46i+22i^2)}{12(1+2i)(-1+i+i^2)}, \frac{8-17i-14i^2}{12(-1+i+i^2)}, \frac{(3+2i)(-1+i+4i^2)}{12(1+2i)(-1+i+i^2)} \right) \end{aligned}$$

Appendix A.2.2. Fifth order interpolation weights

- Positive (right) weights:

$$\begin{aligned} S_0^{5+} :: \quad (w_{i,0,-2}^{5+}, w_{i,0,-1}^{5+}, w_{i,0,0}^{5+}, w_{i,0,+1}^{5+}, w_{i,0,+2}^{5+}) &= \left(\frac{(-5+2i)(4-10i^2+3i^4)}{30(-1+2i)(12+16i-13i^2-6i^3+3i^4)}, \right. \\ &\quad -\frac{(-3+2i)(164+45i-380i^2-75i^3+78i^4)}{120(-1+2i)(12+16i-13i^2-6i^3+3i^4)}, \frac{1276+1395i-1300i^2-525i^3+282i^4}{120(12+16i-13i^2-6i^3+3i^4)}, \frac{(1+2i)(-228+465i-60i^2-175i^3+54i^4)}{40(-1+2i)(12+16i-13i^2-6i^3+3i^4)}, \\ &\quad \left. -\frac{(3+2i)(-12+15i+20i^2-25i^3+6i^4)}{40(-1+2i)(12+16i-13i^2-6i^3+3i^4)} \right) \end{aligned}$$

- Middle weights:

$$\begin{aligned} S_0^{5M} :: \quad (w_{i,0,-2}^{5M}, w_{i,0,-1}^{5M}, w_{i,0,0}^{5M}, w_{i,0,+1}^{5M}, w_{i,0,+2}^{5M}) &= \\ &= \left(\frac{3(-5+2i)}{640(-1+2i)}, -\frac{29(-3+2i)}{480(-1+2i)}, \frac{1067}{960}, \frac{29+58i}{480-960i}, \frac{3(3+2i)}{640(-1+2i)} \right) \end{aligned}$$

- Negative (left) weights:

$$S_0^{5-} :: (w_{i,0,-2}^{5-}, w_{i,0,-1}^{5-}, w_{i,0,0}^{5-}, w_{i,0,+1}^{5-}, w_{i,0,+2}^{5-}) = \left(-\frac{(-5+2i)(4-4i-19i^2+i^3+6i^4)}{40(-1+2i)(12+16i-13i^2-6i^3+3i^4)}, \right. \\ \left. \frac{(-3+2i)(56-36i-261i^2-41i^3+54i^4)}{40(-1+2i)(12+16i-13i^2-6i^3+3i^4)}, \frac{1128+1652i-1183i^2-603i^3+282i^4}{120(12+16i-13i^2-6i^3+3i^4)}, -\frac{(1+2i)(-168+628i-137i^2-237i^3+78i^4)}{120(-1+2i)(12+16i-13i^2-6i^3+3i^4)}, \right. \\ \left. \frac{(3+2i)(-3+8i+8i^2-12i^3+3i^4)}{30(-1+2i)(12+16i-13i^2-6i^3+3i^4)} \right)$$

Appendix A.2.3. Optimal weights

The (θ, z) -directional optimal weights are exactly the same as of the Cartesian coordinates given in subsection Appendix A.1.3. However, the optimal weights in cylindrical-radial (R) coordinates are different, as given below. It is observed that the weights are not mirror-symmetric and are independent of the grid spacing but depend only on the index number i , where $i = \frac{R_{i+\frac{1}{2}}}{\Delta R}$.

- Positive (right) weights:: $(C_{i,0}^+, C_{i,1}^+, C_{i,2}^+) = \left(\frac{2(-3+2i)(1-3i+i^2)(4-10i^2+3i^4)}{5(-1+2i)(4-9i+4i^2)(12+16i-13i^2-6i^3+3i^4)}, \right. \\ \left. \frac{3(-1-i+i^2)(96-192i-191i^2+500i^3-83i^4-154i^5+48i^6)}{10(-1+2i^2)(4-9i+4i^2)(12+16i-13i^2-6i^3+3i^4)}, \frac{3(1+2i)(-1+i+i^2)(-12+15i+20i^2-25i^3+6i^4)}{10(-1+2i)(-1+2i^2)(12+16i-13i^2-6i^3+3i^4)} \right)$
- Middle weights:: $(C_{i,0}^M, C_{i,1}^M, C_{i,2}^M) = \left(-\frac{9(-3+11i-9i^2+2i^3)}{80(-1+2i)(-1-i+i^2)}, \frac{22+49i-49i^2}{40(1+i-i^2)}, -\frac{9(1+2i)(-1+i+i^2)}{80(-1+2i)(-1-i+i^2)} \right)$
- Negative (left) weights:: $(C_{i,0}^-, C_{i,1}^-, C_{i,2}^-) = \left(\frac{3(-3+2i)(1-3i+i^2)(4-4i-19i^2+i^3+6i^4)}{10(-1+2i)(1-4i+2i^2)(12+16i-13i^2-6i^3+3i^4)}, \right. \\ \left. \frac{3(-1-i+i^2)(24-112i-9i^2+412i^3-133i^4-134i^5+48i^6)}{10(1-4i+2i^2)(-1+i+4i^2)(12+16i-13i^2-6i^3+3i^4)}, \frac{2(1+2i)(-1+i+i^2)(-3+8i+8i^2-12i^3+3i^4)}{5(-1+2i)(-1+i+4i^2)(12+16i-13i^2-6i^3+3i^4)} \right)$

Appendix A.2.4. Weights for interface value integration

For 1D/2D cases, one-dimensional Jacobian is the same as of source-term integration, given in table 1. For these cases, the weights for integration in θ and z direction will be the same as given in Appendix A.1.4. However, its value in R direction will be different as given below:

- Fifth order (all middle values):: $(w_{i,-2}^M, w_{i,-1}^M, w_{i,0}^M, w_{i,+1}^M, w_{i,+2}^M) = \left(\frac{17(2\Delta R - R_i)}{5760R_i}, -\frac{77(\Delta R - R_i)}{1440R_i}, \frac{863}{960}, \frac{77(\Delta R + R_i)}{1440R_i}, -\frac{17(2\Delta R + R_i)}{5760R_i} \right)$
- Sixth order (all interface values):: $(w_{i,-5/2}^+, w_{i,-3/2}^+, w_{i,-1/2}^+, w_{i,+1/2}^-, w_{i,+3/2}^-, w_{i,+5/2}^-) = \left(\frac{154 - \frac{3\Delta R}{R_i}}{20160}, -\frac{31}{480} + \frac{43\Delta R}{20160R_i}, \frac{401}{720} - \frac{299\Delta R}{3360R_i}, \frac{401}{720} + \frac{299\Delta R}{3360R_i}, -\frac{31}{480} - \frac{43\Delta R}{20160R_i}, \frac{154 + \frac{3\Delta R}{R_i}}{20160} \right)$

From table 2, it is clear that for 3D cases, one-dimensional Jacobian is altered, therefore, the weights will be different. For $(r-z)$ and $(\theta-z)$ coordinates, the one-dimensional Jacobians are unity for both the sweeps. But for $(r-\theta)$ the r -directional integration can be performed by the weights given earlier in this section and for θ -directional weights are the same as given in Appendix A.1.4.

Appendix A.2.5. Weights for source term integration

For source term integration, the one-dimensional Jacobian is the original value as summarized in table 1. But in this case, regularization is performed to get rid of '1/R' factor. Apart from the radial integration, the weights for θ - and z -directional integration are the same as of Cartesian weights given in Appendix A.1.5. Weights for r -directional integration are given below:

- Three point based Simpson quadrature (2 interface, 1 middle values)::

1. Original weights: $(w_{i,-1/2}^+, w_{i,0}^M, w_{i,+1/2}^-) = \left(\frac{1}{6} - \frac{\Delta R}{12R_i}, \frac{2}{3}, \frac{\Delta R + 2R_i}{12R_i}\right)$
2. Regularized weights: $(\hat{w}_{i,-1/2}^+, \hat{w}_{i,0}^M, \hat{w}_{i,+1/2}^-) = \left(\frac{1}{6R_i}, \frac{2}{3R_i}, \frac{1}{6R_i}\right)$

- Fifth order (all middle values)::

1. Original weights: Ref. to Appendix A.2.4
2. Regularized weights: $(\hat{w}_{i,-2}^M, \hat{w}_{i,-1}^M, \hat{w}_{i,0}^M, \hat{w}_{i,+1}^M, \hat{w}_{i,+2}^M) = \left(-\frac{17}{5760R_i}, \frac{77}{1440R_i}, \frac{863}{960R_i}, \frac{77}{1440R_i}, -\frac{17}{5760R_i}\right)$

- Sixth order (all interface values)::

1. Original weights: Ref. to Appendix A.2.4
2. Regularized weights: $(\hat{w}_{i,-5/2}^+, \hat{w}_{i,-3/2}^+, \hat{w}_{i,-1/2}^+, \hat{w}_{i,+1/2}^-, \hat{w}_{i,+3/2}^-, \hat{w}_{i,+5/2}^-) = \left(\frac{11}{1440R_i}, -\frac{31}{480R_i}, \frac{401}{720R_i}, \frac{401}{720R_i}, -\frac{31}{480R_i}, \frac{11}{1440R_i}\right)$

Appendix A.3. Spherical coordinates

Appendix A.3.1. Linear weights

In the case of spherical coordinate (ϕ), the linear weights are obtained by putting $m = 0$ in Eq. (26) and then inverting the β -matrix in Eq. (24). For this case, the weights are the same as in the Cartesian coordinates given in the subsection Appendix A.1.1. However, for the case of radial coordinate (r), $m = 2$ is used and the weights are given below, where $i = \frac{r_{i+\frac{1}{2}}}{\Delta r}$ is independent of the grid spacing and depends only on the index number of the grid. Again, in the vanishing curvature ($R \rightarrow \infty$ and therefore $i \rightarrow \infty$), the linear weights of the conventional WENO reconstruction in Cartesian coordinates can be recovered. Also, for the case of spherical–meridional coordinate (θ), analytical solutions are highly complex, therefore, application of direct numerical inversion is advised.

- Positive (right) weights:

$$\begin{aligned}
 S_0^{3+}(i-2, i-1, i) :: \quad & (w_{i,0,-2}^{3+}, w_{i,0,-1}^{3+}, w_{i,0,0}^{3+}) = \left(\frac{(19-15i+3i^2)(12-48i+72i^2-45i^3+10i^4)}{9(36-198i+471i^2-540i^3+315i^4-90i^5+10i^6)}, \right. \\
 & \left. -\frac{(7-9i+3i^2)(219-768i+963i^2-450i^3+70i^4)}{18(36-198i+471i^2-540i^3+315i^4-90i^5+10i^6)}, \frac{(1-3i+3i^2)(1725-3552i+2709i^2-900i^3+110i^4)}{18(36-198i+471i^2-540i^3+315i^4-90i^5+10i^6)} \right) \\
 S_1^{3+}(i-1, i, i+1) :: \quad & (w_{i,1,-1}^{3+}, w_{i,1,0}^{3+}, w_{i,1,+1}^{3+}) = \left(-\frac{(7-9i+3i^2)(3-9i^2+10i^4)}{18(4-6i-9i^2+20i^3+15i^4-30i^5+10i^6)}, \right. \\
 & \left. \frac{(1-3i+3i^2)(69+96i-63i^2-90i^3+50i^4)}{18(4-6i-9i^2+20i^3+15i^4-30i^5+10i^6)}, \frac{(1+3i+3i^2)(12-48i+72i^2-45i^3+10i^4)}{9(4-6i-9i^2+20i^3+15i^4-30i^5+10i^6)} \right) \\
 S_2^{3+}(i, i+1, i+2) :: \quad & (w_{i,2,0}^{3+}, w_{i,2,+1}^{3+}, w_{i,2,+2}^{3+}) = \left(\frac{(1-3i+3i^2)(12+48i+72i^2+45i^3+10i^4)}{9(4+6i-9i^2-20i^3+15i^4+30i^5+10i^6)}, \right. \\
 & \left. \frac{(1+3i+3i^2)(69-96i-63i^2+90i^3+50i^4)}{18(4+6i-9i^2-20i^3+15i^4+30i^5+10i^6)}, -\frac{(7+9i+3i^2)(3-9i^2+10i^4)}{18(4+6i-9i^2-20i^3+15i^4+30i^5+10i^6)} \right)
 \end{aligned}$$

- Middle weights:

$$\begin{aligned}
 S_0^{3M}(i-2, i-1, i) :: \quad & (w_{i,0,-2}^{3M}, w_{i,0,-1}^{3M}, w_{i,0,0}^{3M}) = \left(-\frac{(19-15i+3i^2)(-20+58i-21i^2-20i^3+10i^4)}{72(36-198i+471i^2-540i^3+315i^4-90i^5+10i^6)}, \right. \\
 & \left. \frac{(7-9i+3i^2)(-223+590i-222i^2-40i^3+20i^4)}{72(36-198i+471i^2-540i^3+315i^4-90i^5+10i^6)}, \frac{(1-3i+3i^2)(3773-7672i+5781i^2-1900i^3+230i^4)}{72(36-198i+471i^2-540i^3+315i^4-90i^5+10i^6)} \right) \\
 S_1^{3M}(i-1, i, i+1) :: \quad & (w_{i,1,-1}^{3M}, w_{i,1,0}^{3M}, w_{i,1,+1}^{3M}) = \left(-\frac{(7-9i+3i^2)(7+4i-21i^2-20i^3+10i^4)}{72(4-6i-9i^2+20i^3+15i^4-30i^5+10i^6)}, \right. \\
 & \left. \frac{(1-3i+3i^2)(317+482i-222i^2-520i^3+260i^4)}{72(4-6i-9i^2+20i^3+15i^4-30i^5+10i^6)}, -\frac{(1+3i+3i^2)(-20+58i-21i^2-20i^3+10i^4)}{72(4-6i-9i^2+20i^3+15i^4-30i^5+10i^6)} \right) \\
 S_2^{3M}(i, i+1, i+2) :: \quad & (w_{i,2,0}^{3M}, w_{i,2,+1}^{3M}, w_{i,2,+2}^{3M}) = \left(\frac{(1-3i+3i^2)(212+890i+1461i^2+980i^3+230i^4)}{72(4+6i-9i^2-20i^3+15i^4+30i^5+10i^6)}, \right. \\
 & \left. \frac{(1+3i+3i^2)(125-106i-222i^2-40i^3+20i^4)}{72(4+6i-9i^2-20i^3+15i^4+30i^5+10i^6)}, -\frac{(7+9i+3i^2)(7+4i-21i^2-20i^3+10i^4)}{72(4+6i-9i^2-20i^3+15i^4+30i^5+10i^6)} \right)
 \end{aligned}$$

- Negative (left) weights:

$$\begin{aligned}
S_0^{3-}(i-2, i-1, i) &:: (w_{i,0,-2}^{3-}, w_{i,0,-1}^{3-}, w_{i,0,0}^{3-}) = \left(-\frac{(19-15i+3i^2)(4-22i+51i^2-40i^3+10i^4)}{18(36-198i+471i^2-540i^3+315i^4-90i^5+10i^6)}, \right. \\
&\quad \left. \frac{(7-9i+3i^2)(50-248i+507i^2-290i^3+50i^4)}{18(36-198i+471i^2-540i^3+315i^4-90i^5+10i^6)}, \frac{(1-3i+3i^2)(187-367i+267i^2-85i^3+10i^4)}{9(36-198i+471i^2-540i^3+315i^4-90i^5+10i^6)} \right) \\
S_1^{3-}(i-1, i, i+1) &:: (w_{i,1,-1}^{3-}, w_{i,1,0}^{3-}, w_{i,1,+1}^{3-}) = \left(\frac{(7-9i+3i^2)(1-i-3i^2+5i^3+10i^4)}{9(4-6i-9i^2+20i^3+15i^4-30i^5+10i^6)}, \right. \\
&\quad \left. \frac{(1-3i+3i^2)(62+100i-33i^2-110i^3+50i^4)}{18(4-6i-9i^2+20i^3+15i^4-30i^5+10i^6)}, -\frac{(1+3i+3i^2)(4-22i+51i^2-40i^3+10i^4)}{18(4-6i-9i^2+20i^3+15i^4-30i^5+10i^6)} \right) \\
S_2^{3-}(i, i+1, i+2) &:: (w_{i,2,0}^{3-}, w_{i,2,+1}^{3-}, w_{i,2,+2}^{3-}) = \left(\frac{(1-3i+3i^2)(92+394i+669i^2+460i^3+110i^4)}{18(4+6i-9i^2-20i^3+15i^4+30i^5+10i^6)}, \right. \\
&\quad \left. -\frac{(1+3i+3i^2)(34-88i+33i^2+170i^3+70i^4)}{18(4+6i-9i^2-20i^3+15i^4+30i^5+10i^6)}, \frac{(7+9i+3i^2)(1-i-3i^2+5i^3+10i^4)}{9(4+6i-9i^2-20i^3+15i^4+30i^5+10i^6)} \right)
\end{aligned}$$

Appendix A.3.2. Fifth order interpolation weights

- Positive (right) weights:

$$\begin{aligned}
S_0^{5+} &:: (w_{i,0,-2}^{5+}, w_{i,0,-1}^{5+}, w_{i,0,0}^{5+}, w_{i,0,+1}^{5+}, w_{i,0,+2}^{5+}) = \\
&\left(\frac{(19-15i+3i^2)(16-60i^2+94i^4-45i^6+7i^8)}{90(48-48i-164i^2+200i^3+390i^4-399i^5-161i^6+210i^7-35i^9+7i^{10})}, \right. \\
&\quad -\frac{(7-9i+3i^2)(508+240i-1740i^2-795i^3+2417i^4+930i^5-780i^6-175i^7+91i^8)}{180(48-48i-164i^2+200i^3+390i^4-399i^5-161i^6+210i^7-35i^9+7i^{10})}, \\
&\quad \frac{(1-3i+3i^2)(8132+15120i-5700i^2-20325i^3+3863i^4+8670i^5-1800i^6-1225i^7+329i^8)}{180(48-48i-164i^2+200i^3+390i^4-399i^5-161i^6+210i^7-35i^9+7i^{10})}, \\
&\quad \frac{(1+3i+3i^2)(4212-15120i+16560i^2+1275i^3-11517i^4+4350i^5+1620i^6-1225i^7+189i^8)}{180(48-48i-164i^2+200i^3+390i^4-399i^5-161i^6+210i^7-35i^9+7i^{10})}, \\
&\quad \left. -\frac{(7+9i+3i^2)(108-240i-120i^2+645i^3-223i^4-510i^5+510i^6-175i^7+21i^8)}{180(48-48i-164i^2+200i^3+390i^4-399i^5-161i^6+210i^7-35i^9+7i^{10})} \right)
\end{aligned}$$

- Middle weights:

$$\begin{aligned}
S_0^{5M} &:: (w_{i,0,-2}^{5M}, w_{i,0,-1}^{5M}, w_{i,0,0}^{5M}, w_{i,0,+1}^{5M}, w_{i,0,+2}^{5M}) = \\
&\left(\frac{(19-15i+3i^2)(176+128i-660i^2-752i^3+562i^4+468i^5-183i^6-84i^7+21i^8)}{1920(48-48i-164i^2+200i^3+390i^4-399i^5-161i^6+210i^7-35i^9+7i^{10})}, \right. \\
&\quad -\frac{(7-9i+3i^2)(9972+10866i-30895i^2-48744i^3+13939i^4+22846i^5-4576i^6-3248i^7+812i^8)}{5760(48-48i-164i^2+200i^3+390i^4-399i^5-161i^6+210i^7-35i^9+7i^{10})}, \\
&\quad \frac{(1-3i+3i^2)(314028+637134i-104105i^2-911256i^3+83561i^4+404654i^5-65174i^6-59752i^7+14938i^8)}{5760(48-48i-164i^2+200i^3+390i^4-399i^5-161i^6+210i^7-35i^9+7i^{10})}, \\
&\quad -\frac{(1+3i+3i^2)(-29028+70866i+20855i^2-75744i^3+2689i^4+27346i^5-4576i^6-3248i^7+812i^8)}{5760(48-48i-164i^2+200i^3+390i^4-399i^5-161i^6+210i^7-35i^9+7i^{10})}, \\
&\quad \left. \frac{(7+9i+3i^2)(-324+378i+1215i^2-752i^3-1313i^4+1218i^5-183i^6-84i^7+21i^8)}{1920(48-48i-164i^2+200i^3+390i^4-399i^5-161i^6+210i^7-35i^9+7i^{10})} \right)
\end{aligned}$$

- Negative (left) weights:

$$\begin{aligned}
S_0^{5-} &:: (w_{i,0,-2}^{5-}, w_{i,0,-1}^{5-}, w_{i,0,0}^{5-}, w_{i,0,+1}^{5-}, w_{i,0,+2}^{5-}) = \\
&\left(-\frac{(19-15i+3i^2)(16-16i-60i^2+96i^3+222i^4-51i^5-127i^6+7i^7+21i^8)}{180(48-48i-164i^2+200i^3+390i^4-399i^5-161i^6+210i^7-35i^9+7i^{10})}, \right. \\
&\quad \left. \frac{(7-9i+3i^2)(344-164i-1350i^2+1184i^3+4888i^4+1071i^5-1663i^6-287i^7+189i^8)}{180(48-48i-164i^2+200i^3+390i^4-399i^5-161i^6+210i^7-35i^9+7i^{10})} \right),
\end{aligned}$$

$$\begin{aligned} & \frac{(1-3i+3i^2)(7064+15196i-310i^2-21376i^3+368i^4+9431i^5-1163i^6-1407i^7+329i^8)}{180(48-48i-164i^2+200i^3+390i^4-399i^5-161i^6+210i^7-35i^9+7i^{10})}, \\ & - \frac{(1+3i+3i^2)(696-3516i+6850i^2-1544i^3-4388i^4+2329i^5+543i^6-553i^7+91i^8)}{180(48-48i-164i^2+200i^3+390i^4-399i^5-161i^6+210i^7-35i^9+7i^{10})}, \\ & \left. \frac{(7+9i+3i^2)(12-42i+25i^2+132i^3-91i^4-122i^5+151i^6-56i^7+7i^8)}{90(48-48i-164i^2+200i^3+390i^4-399i^5-161i^6+210i^7-35i^9+7i^{10})} \right) \end{aligned}$$

Appendix A.3.3. Optimal weights

The ϕ -directional optimal weights are the same as of the Cartesian ones, given in subsection Appendix A.1.3. Moreover, the spherical-meridional θ -directional optimal weights are evaluated by direct numerical operation since the analytical values for that case are highly complicated. Even the analytical values of the optimal weights for spherical-radial (r) coordinates are highly intricate but are grid spacing independent and are given below for the uniform grid, where the index number $i = \frac{r_{i+\frac{1}{2}}}{\Delta r}$.

- Positive (right) weights:: $(C_{i,0}^+, C_{i,1}^+, C_{i,2}^+) =$

$$\left(\begin{aligned} & \frac{(36-198i+471i^2-540i^3+315i^4-90i^5+10i^6)(16-60i^2+94i^4-45i^6+7i^8)}{10(12-48i+72i^2-45i^3+10i^4)(48-48i-164i^2+200i^3+390i^4-399i^5-161i^6+210i^7-35i^9+7i^{10})}, \\ & \frac{(4-6i-9i^2+20i^3+15i^4-30i^5+10i^6)(2592-9216i+1908i^2+29520i^3-27762i^4-36204i^5+61932i^6 \dots}{10(3-9i^2+10i^4)(12-48i+72i^2-45i^3+10i^4)(48-48i-164i^2+200i^3+390i^4-399i^5-161i^6+210i^7-35i^9+7i^{10})} \\ & \dots - 6675i^7 - 29126i^8 + 12558i^9 + 3036i^{10} - 2695i^{11} + 420i^{12})}{10(3-9i^2+10i^4)(12-48i+72i^2-45i^3+10i^4)(48-48i-164i^2+200i^3+390i^4-399i^5-161i^6+210i^7-35i^9+7i^{10})}, \\ & \frac{(4+6i-9i^2-20i^3+15i^4+30i^5+10i^6)(108-240i-120i^2+645i^3-223i^4-510i^5+510i^6-175i^7+21i^8)}{10(3-9i^2+10i^4)(48-48i-164i^2+200i^3+390i^4-399i^5-161i^6+210i^7-35i^9+7i^{10})} \end{aligned} \right)$$
- Middle weights:: $(C_{i,0}^M, C_{i,1}^M, C_{i,2}^M) =$

$$\left(\begin{aligned} & - \frac{3(36-198i+471i^2-540i^3+315i^4-90i^5+10i^6)(176+128i-660i^2-752i^3+562i^4+468i^5-183i^6-84i^7+21i^8)}{80(-20+58i-21i^2-20i^3+10i^4)(48-48i-164i^2+200i^3+390i^4-399i^5-161i^6+210i^7-35i^9+7i^{10})}, \\ & \frac{(4-6i-9i^2+20i^3+15i^4-30i^5+10i^6)(-81696+135168i+487832i^2-473176i^3-1302479i^4+832366i^5+1162664i^6-754472i^7}{(80(7+4i-21i^2-20i^3+10i^4)(-20+58i-21i^2-20i^3+10i^4)(48-48i-164i^2+200i^3+390i^4-399i^5-161i^6+210i^7-35i^9+7i^{10}))} \\ & - 362767i^8 + 292130i^9 + 17034i^{10} - 41160i^{11} + 6860i^{12})}{(80(7+4i-21i^2-20i^3+10i^4)(-20+58i-21i^2-20i^3+10i^4)(48-48i-164i^2+200i^3+390i^4-399i^5-161i^6+210i^7-35i^9+7i^{10}))}, \\ & - \frac{3(4+6i-9i^2-20i^3+15i^4+30i^5+10i^6)(-324+378i+1215i^2-752i^3-1313i^4+1218i^5-183i^6-84i^7+21i^8)}{80(7+4i-21i^2-20i^3+10i^4)(48-48i-164i^2+200i^3+390i^4-399i^5-161i^6+210i^7-35i^9+7i^{10})} \end{aligned} \right)$$
- Negative (left) weights:: $(C_{i,0}^-, C_{i,1}^-, C_{i,2}^-) =$

$$\left(\begin{aligned} & \frac{(36-198i+471i^2-540i^3+315i^4-90i^5+10i^6)(16-16i-60i^2+96i^3+222i^4-51i^5-127i^6+7i^7+21i^8)}{10(4-22i+51i^2-40i^3+10i^4)(48-48i-164i^2+200i^3+390i^4-399i^5-161i^6+210i^7-35i^9+7i^{10})}, \\ & \frac{(4-6i-9i^2+20i^3+15i^4-30i^5+10i^6)(17856-78336i+24528i^2+525848i^3-493806i^4-1868490i^5+2594599i^6+3894831i^7 \dots}{(10(4-22i+51i^2-40i^3+10i^4)(1-i-3i^2+5i^3+10i^4)(69+96i-63i^2-90i^3+50i^4)(48-48i-164i^2+200i^3+390i^4-399i^5-161i^6+210i^7-35i^9+7i^{10}))} \\ & \dots - 4959771i^8 - 3980631i^9 + 5852829i^{10} + 327519i^{11} - 2477843i^{12} + 642525i^{13} + 299640i^{14} - 163450i^{15} + 21000i^{16})}{(10(4-22i+51i^2-40i^3+10i^4)(1-i-3i^2+5i^3+10i^4)(69+96i-63i^2-90i^3+50i^4)(48-48i-164i^2+200i^3+390i^4-399i^5-161i^6+210i^7-35i^9+7i^{10}))}, \\ & \frac{(4+6i-9i^2-20i^3+15i^4+30i^5+10i^6)(12-42i+25i^2+132i^3-91i^4-122i^5+151i^6-56i^7+7i^8)}{10(1-i-3i^2+5i^3+10i^4)(48-48i-164i^2+200i^3+390i^4-399i^5-161i^6+210i^7-35i^9+7i^{10})} \end{aligned} \right)$$

Appendix A.3.4. Weights for interface value integration

In 1D/2D case, original weights for interpolation might be used according to the situation. In z coordinates, the weights are the same as of Cartesian grids given in Appendix A.1.4. Weights for θ –directional integration are extremely complex and advised to be computed numerically. r –directional integration weights are given below:

- Fifth order (all middle values):: $(w_{i,-2}^M, w_{i,-1}^M, w_{i,0}^M, w_{i,+1}^M, w_{i,+2}^M) =$

$$\left(\frac{-69\Delta r^2 + 1904\Delta r r_i - 476r_i^2}{13440(\Delta r^2 + 12r_i^2)}, \frac{321\Delta r^2 - 4312\Delta r r_i + 2156r_i^2}{3360(\Delta r^2 + 12r_i^2)}, \frac{1835\Delta r^2 + 24164r_i^2}{2240(\Delta r^2 + 12r_i^2)}, \right.$$

$$\left. \frac{321\Delta r^2 + 4312\Delta r r_i + 2156r_i^2}{3360(\Delta r^2 + 12r_i^2)}, -\frac{69\Delta r^2 + 1904\Delta r r_i + 476r_i^2}{13440(\Delta r^2 + 12r_i^2)} \right)$$
- Sixth order (all interface values):: $(w_{i,-5/2}^+, w_{i,-3/2}^+, w_{i,-1/2}^+, w_{i,+1/2}^-, w_{i,+3/2}^-, w_{i,+5/2}^-) =$

$$\left(\frac{15\Delta r^2 - 12\Delta r r_i + 308r_i^2}{3360(\Delta r^2 + 12r_i^2)}, \frac{-129\Delta r^2 + 172\Delta r r_i - 2604r_i^2}{3360(\Delta r^2 + 12r_i^2)}, \frac{897\Delta r^2 - 3588\Delta r r_i + 11228r_i^2}{1680(\Delta r^2 + 12r_i^2)}, \right.$$

$$\left. \frac{897\Delta r^2 + 3588\Delta r r_i + 11228r_i^2}{1680(\Delta r^2 + 12r_i^2)}, -\frac{129\Delta r^2 + 172\Delta r r_i + 2604r_i^2}{3360(\Delta r^2 + 12r_i^2)}, \frac{15\Delta r^2 + 12\Delta r r_i + 308r_i^2}{3360(\Delta r^2 + 12r_i^2)} \right)$$

For 3D cases, one–dimensional Jacobian values are given in table 2. For $(r - \theta)$ and $(r - \phi)$ planes, the one directional sweeps in r direction can be evaluated from the weights given in Appendix A.2.4 and θ – or ϕ –directional integration weights given in Appendix A.1.4. For $(\theta - \phi)$ planes, analytical values are extremely complex and thus, require direct numerical procedure.

Appendix A.3.5. Weights for source term integration

The original one–dimensional Jacobian values for this case are given in table 1. The original and regularized quadrature values in ϕ direction can be computed from Appendix A.1.5, θ direction by direct numerical operation, and radial (r) direction from the weights given below:

- Three point based Simpson quadrature (2 interface, 1 middle values)::

1. Original weights: $(w_{i,-1/2}^+, w_{i,0}^M, w_{i,+1/2}^-) =$

$$\left(\frac{3\Delta r^2 - 20\Delta r r_i + 20r_i^2}{10\Delta r^2 + 120r_i^2}, \frac{2(\Delta r^2 + 20r_i^2)}{5(\Delta r^2 + 12r_i^2)}, \frac{3\Delta r^2 + 20\Delta r r_i + 20r_i^2}{10\Delta r^2 + 120r_i^2} \right)$$

$$2. \text{ Regularized weights: } (\hat{w}_{i,-1/2}^+, \hat{w}_{i,0}^M, \hat{w}_{i,+1/2}^-) = \left(-\frac{\Delta r - 2r_i}{\Delta r^2 + 12r_i^2}, \frac{8r_i}{\Delta r^2 + 12r_i^2}, \frac{\Delta r + 2r_i}{\Delta r^2 + 12r_i^2} \right)$$

- Fifth order (all middle values)::

1. Original weights: Ref. to Appendix A.3.4

$$2. \text{ Regularized weights: } (\hat{w}_{i,-2}^M, \hat{w}_{i,-1}^M, \hat{w}_{i,0}^M, \hat{w}_{i,+1}^M, \hat{w}_{i,+2}^M) = \left(\frac{17(2\Delta r - r_i)}{480(\Delta r^2 + 12r_i^2)}, -\frac{77(\Delta r - r_i)}{120(\Delta r^2 + 12r_i^2)}, \frac{863r_i}{80(\Delta r^2 + 12r_i^2)}, \frac{77(\Delta r + r_i)}{120(\Delta r^2 + 12r_i^2)}, -\frac{17(2\Delta r + r_i)}{480(\Delta r^2 + 12r_i^2)} \right)$$

- Sixth order (all interface values)::

1. Original weights: Ref. to Appendix A.3.4

$$2. \text{ Regularized weights: } (\hat{w}_{i,-5/2}^+, \hat{w}_{i,-3/2}^+, \hat{w}_{i,-1/2}^+, \hat{w}_{i,+1/2}^-, \hat{w}_{i,+3/2}^-, \hat{w}_{i,+5/2}^-) = \left(\frac{-3\Delta r + 154r_i}{1680(\Delta r^2 + 12r_i^2)}, \frac{43\Delta r - 1302r_i}{1680(\Delta r^2 + 12r_i^2)}, \frac{-897\Delta r + 5614r_i}{840(\Delta r^2 + 12r_i^2)}, \frac{897\Delta r + 5614r_i}{840(\Delta r^2 + 12r_i^2)}, -\frac{43\Delta r + 1302r_i}{1680(\Delta r^2 + 12r_i^2)}, \frac{3\Delta r + 154r_i}{1680(\Delta r^2 + 12r_i^2)} \right)$$

References

References

- [1] V. A. Titarev, E. F. Toro, Finite-volume weno schemes for three-dimensional conservation laws, Journal of Computational Physics 201 (1) (2004) 238–260.
- [2] A. Mignone, High-order conservative reconstruction schemes for finite volume methods in cylindrical and spherical coordinates, Journal of Computational Physics 270 (2014) 784–814.
- [3] G.-S. Jiang, C.-W. Shu, Efficient implementation of weighted eno schemes, Journal of computational physics 126 (1) (1996) 202–228.
- [4] X.-D. Liu, S. Osher, T. Chan, Weighted essentially non-oscillatory schemes, Journal of computational physics 115 (1) (1994) 200–212.

- [5] D. S. Balsara, C.-W. Shu, Monotonicity preserving weighted essentially non-oscillatory schemes with increasingly high order of accuracy, *Journal of Computational Physics* 160 (2) (2000) 405–452.
- [6] C.-W. Shu, High-order finite difference and finite volume weno schemes and discontinuous galerkin methods for cfd, *International Journal of Computational Fluid Dynamics* 17 (2) (2003) 107–118.
- [7] G.-S. Jiang, C.-c. Wu, A high-order weno finite difference scheme for the equations of ideal magnetohydrodynamics, *Journal of Computational Physics* 150 (2) (1999) 561–594.
- [8] D. S. Balsara, Divergence-free reconstruction of magnetic fields and weno schemes for magnetohydrodynamics, *Journal of Computational Physics* 228 (14) (2009) 5040–5056.
- [9] D. S. Balsara, T. Rumpf, M. Dumbser, C.-D. Munz, Efficient, high accuracy ader-weno schemes for hydrodynamics and divergence-free magnetohydrodynamics, *Journal of Computational Physics* 228 (7) (2009) 2480–2516.
- [10] J. Casper, H. Atkins, A finite-volume high-order eno scheme for two-dimensional hyperbolic systems, *Journal of Computational Physics* 106 (1) (1993) 62–76.
- [11] P. Colella, P. R. Woodward, The piecewise parabolic method (ppm) for gas-dynamical simulations, *Journal of computational physics* 54 (1) (1984) 174–201.
- [12] P. Colella, M. D. Sekora, A limiter for ppm that preserves accuracy at smooth extrema, *Journal of Computational Physics* 227 (15) (2008) 7069–7076.
- [13] P. McCorquodale, P. Colella, A high-order finite-volume method for conservation laws on locally refined grids, *Communications in Applied Mathematics and Computational Science* 6 (1) (2011) 1–25.

- [14] N. K. Yamaleev, M. H. Carpenter, A systematic methodology for constructing high-order energy stable weno schemes, *Journal of Computational Physics* 228 (11) (2009) 4248–4272.
- [15] D. S. Balsara, S. Garain, C.-W. Shu, An efficient class of weno schemes with adaptive order, *Journal of Computational Physics* 326 (2016) 780–804.
- [16] J. Luo, K. Xu, A high-order multidimensional gas-kinetic scheme for hydrodynamic equations, *Sci. China, Technol. Sci* 56 (10) (2013) 2370–2384.
- [17] R. Zhang, M. Zhang, C.-W. Shu, On the order of accuracy and numerical performance of two classes of finite volume weno schemes, *Communications in Computational Physics* 9 (3) (2011) 807–827.
- [18] P. Buchmüller, C. Helzel, Improved accuracy of high-order weno finite volume methods on cartesian grids, *Journal of Scientific Computing* 61 (2) (2014) 343–368.
- [19] E. F. Toro, *Riemann solvers and numerical methods for fluid dynamics: a practical introduction*, Springer Science & Business Media, 2013.
- [20] K. Xu, A gas-kinetic bgk scheme for the navier–stokes equations and its connection with artificial dissipation and godunov method, *Journal of Computational Physics* 171 (1) (2001) 289–335.
- [21] K. Xu, J.-C. Huang, A unified gas-kinetic scheme for continuum and rarefied flows, *Journal of Computational Physics* 229 (20) (2010) 7747–7764.
- [22] S. Gottlieb, C.-W. Shu, Total variation diminishing runge-kutta schemes, *Mathematics of computation of the American Mathematical Society* 67 (221) (1998) 73–85.
- [23] V. V. Rusanov, The calculation of the interaction of non-stationary shock waves and obstacles, *USSR Computational Mathematics and Mathematical Physics* 1 (2) (1962) 304–320.

- [24] J. M. Blondin, E. A. Lufkin, The piecewise-parabolic method in curvilinear coordinates, *The Astrophysical Journal Supplement Series* 88 (1993) 589–594.
- [25] E. Johnsen, T. Colonius, Implementation of weno schemes in compressible multicomponent flow problems, *Journal of Computational Physics* 219 (2) (2006) 715–732.
- [26] S. Wang, E. Johnsen, High-order schemes for the euler equations in cylindrical/spherical coordinates, *arXiv preprint arXiv:1701.04834*.
- [27] B. Fryxell, K. Olson, P. Ricker, F. Timmes, M. Zingale, D. Lamb, P. MacNeice, R. Rosner, J. Truran, H. Tufo, Flash: An adaptive mesh hydrodynamics code for modeling astrophysical thermonuclear flashes, *The Astrophysical Journal Supplement Series* 131 (1) (2000) 273.
- [28] G. A. Sod, A survey of several finite difference methods for systems of nonlinear hyperbolic conservation laws, *Journal of computational physics* 27 (1) (1978) 1–31.
- [29] A. Harten, P. D. Lax, B. Van Leer, On upstream differencing and godunov-type schemes for hyperbolic conservation laws, in: *Upwind and High-Resolution Schemes*, Springer, 1997, pp. 53–79.
- [30] B. Van Leer, Towards the ultimate conservative difference scheme. v. a second-order sequel to godunov’s method, *Journal of computational Physics* 32 (1) (1979) 101–136.
- [31] R. W. MacCormack, A numerical method for solving the equations of compressible viscous flow, *AIAA journal* 20 (9) (1982) 1275–1281.
- [32] P. D. Lax, X.-D. Liu, Solution of two-dimensional riemann problems of gas dynamics by positive schemes, *SIAM Journal on Scientific Computing* 19 (2) (1998) 319–340.